

Stellar Populations of Lyman Alpha Emitters at $z = 3 - 4$ Based on Deep Large Area Surveys in the Subaru-SXDS/UKIDSS-UDS Field

Yoshiaki Ono,¹ Masami Ouchi,^{2,3} Kazuhiro Shimasaku,^{1,4} Masayuki Akiyama,⁵ James Dunlop,^{6,7} Duncan Farrah,^{8,9} Janice C. Lee,^{2,10} Ross McLure,⁷ Sadanori Okamura,^{1,4} and Makiko Yoshida¹

¹ Department of Astronomy, Graduate School of Science, The University of Tokyo, Tokyo 113-0033, Japan

² Observatories of the Carnegie Institution of Washington, 813 Santa Barbara Street, Pasadena, CA 91101, USA

³ Carnegie Fellow

⁴ Research Center for the Early Universe, Graduate School of Science, The University of Tokyo, Tokyo 113-0033, Japan

⁵ Astronomical Institute, Graduate School of Science, Tohoku University, Aramaki, Aoba, Sendai 980-8578, Japan

⁶ Department of Physics and Astronomy, University of British Columbia, 6224 Agricultural Road, Vancouver V6T 1Z1, Canada

⁷ SUPA Institute for Astronomy, University of Edinburgh, Royal Observatory, Edinburgh EH9 3HJ, UK

⁸ Department of Astronomy, Cornell University, Ithaca, NY 14853

⁹ Astronomy Centre, University of Sussex, Falmer, Brighton, UK

¹⁰ Hubble Fellow

Accepted 2009 November 11. Received 2009 October 28; in original form 2009 May 20

ABSTRACT

We investigate the stellar populations of Lyman α emitters (LAEs) at $z = 3.1$ and 3.7 in 0.65 deg^2 of the Subaru/*XMM-Newton* Deep Field, based on rest-frame UV-to-optical photometry obtained from the Subaru/*XMM-Newton* Deep Survey, the UKIDSS/Ultra Deep Survey, and the Spitzer legacy survey of the UKIDSS/UDS. Among a total of 302 LAEs (224 for $z = 3.1$ and 78 for $z = 3.7$), only 11 are detected in the K band, i.e., brighter than $K(3\sigma) = 24.1 \text{ mag}$. Eight of the 11 K -detected LAEs are spectroscopically confirmed. In our stellar population analysis, we treat K -detected objects individually, while K -undetected objects are stacked at each redshift. We find that the K -undetected objects, which should closely represent the LAE population as a whole, have low stellar masses of $\sim 10^8 - 10^{8.5} M_\odot$, modest SFRs of $1 - 100 M_\odot \text{ yr}^{-1}$, and modest dust extinction of $E(B - V)_* < 0.2$. The K -detected objects are massive, $M_{\text{star}} \sim 10^9 - 10^{10.5} M_\odot$, and have significant dust extinction with a median of $E(B - V)_* \simeq 0.3$. Four K -detected objects with the reddest spectral energy distributions, two of which are spectroscopically confirmed, are heavily obscured with $E(B - V)_* \sim 0.65$, and their continua resemble those of some local ULIRGs. Interestingly, they have large Lyman α equivalent widths $\simeq 70 - 250 \text{ \AA}$. If these four are excluded, our sample has a weak anti-correlation between Ly α equivalent width and M_{star} . We compare the stellar masses and the specific star formation rates (sSFR) of LAEs with those of Lyman-break galaxies (LBGs), distant red galaxies, submillimetre galaxies, and I - or K -selected galaxies with photometric redshifts of $z_{\text{phot}} \sim 3$. We find that the LAE population is the least massive among all the galaxy populations in question, but with relatively high sSFRs, while NIR-detected LAEs have M_{star} and sSFR similar to LBGs. Our reddest four LAEs have very high sSFRs in spite of large M_{star} , thus occupying a unique region in the M_{star} versus sSFR space.

Key words: cosmology: observations — galaxies: formation — galaxies: evolution — galaxies: high-redshift — galaxies: stellar content —

1 INTRODUCTION

Lyman α emitters (LAEs) are a galaxy population which are common in the high redshift Universe. In the last decade,

many observations have succeeded in detecting LAEs from $z \sim 2$ up to $z \sim 7$, primarily based on narrow-band imaging to isolate Lyman α emission (e.g. Hu et al. 1998; Rhoads et al. 2000; Iye et al. 2006). Over a thousand LAEs are now photometrically or spectroscopically identified (e.g. Hu et al. 2002; Ouchi et al. 2003; Malhotra & Rhoads 2004; Taniguchi et al. 2005; Shimasaku et al. 2006; Kashikawa et al. 2006; Dawson et al. 2007; Murayama et al. 2007; Gronwall et al. 2007; Ouchi et al. 2008).

Most LAEs have relatively faint, blue UV continua and large Ly α equivalent widths (EWs). These properties collectively suggest that they are young star-forming galaxies with low metallicities (e.g. Malhotra & Rhoads 2002). In this sense, they may serve as building blocks of larger galaxies in hierarchical galaxy formation.

Stellar population analysis is helpful to further constrain the nature of LAEs. Recent multiwavelength observations covering near-infrared wavelengths have enabled analysis of the stellar populations of LAEs, and there is growing evidence that not all LAEs are primordial as described above. Table 1 summarises studies of the stellar populations of LAEs, including the work presented here. Gawiser et al. (2007) have performed a stacking analysis of 52 LAEs at $z = 3.1$, and concluded that LAEs have low stellar masses ($\simeq 10^9 M_\odot$), young-age components ($\simeq 20$ Myr), and small dust extinctions ($A_V = 0$) (see also Gawiser et al. 2006; Nilsson et al. 2007). Pirzkal et al. (2007) have studied nine LAEs at $z \sim 5$ found by HST/ACS slitless spectroscopy in the Hubble Ultra Deep Field, to show that these faint LAEs are all very young ($\simeq 1 - 20$ Myr) with low masses ($\simeq 10^6 - 10^8 M_\odot$) and small dust extinctions ($A_V = 0 - 0.6$). On the other hand, Lai et al. (2007) have concentrated on three spectroscopically confirmed LAEs at $z = 5.7$ with IRAC detection, and derived relatively large stellar masses, $\simeq 10^9 - 10^{10} M_\odot$, mild dust extinctions ($E(B - V) \simeq 0.15 - 0.2$), and a wide range of age, $\simeq 5 - 100$ Myr. Lai et al. (2008) have studied both IRAC-detected and undetected LAEs at $z = 3.1$ by the stacking method, to find that LAEs possess wide ranges of age ($\simeq 160$ Myr $- 1.6$ Gyr) and mass ($\simeq 10^8 - 10^{10} M_\odot$) without dust extinction. Finkelstein et al. (2009) have analysed 14 LAEs individually, which are either IRAC-detected or undetected. Their results also show wide ranges of stellar population age ($\simeq 2.5 - 500$ Myr), stellar mass ($\simeq 10^8 - 10^{10} M_\odot$), and dust extinction ($A_{1200} \simeq 0.3 - 5.0$).

However, most of the samples constructed to date are not necessarily large and deep enough to constrain the average stellar populations of LAEs and to study rare, massive LAEs which may be a bridge to more massive and/or evolved objects like LBGs. In addition, correlations between stellar population parameters have not been addressed well.

Recently, Ouchi et al. (2008) have constructed the largest available sample of $z = 3.1$ and 3.7 LAEs in an about 1 deg^2 of the Subaru/*XMM-Newton* Deep Field (SXDF) from deep optical broadband and narrowband data. These large survey data enable us not only to find many massive LAEs, but also to place better constraints on less massive (i.e., average) LAEs using stacking analysis. Our sample used in this study consists of 224 (78) LAEs at $z = 3.1$ (3.7) covered by deep *JHK* images taken with the UKIRT/WFCAM from UKIDSS Ultra Deep Survey (UDS; Warren et al. 2007) and $3.6 - 8.0 \mu\text{m}$ images taken with the Spitzer/IRAC from the Spitzer legacy survey of

the UDS field (SpUDS; PI: J. Dunlop)¹, among which 5 (6) are detected in the *K* band (i.e., brighter than the 3σ detection limit of the *K*-band image). The *K* band corresponds to the rest-frame *V* and *B* bands at $z = 3.1$ and 3.7 , respectively. For *K*-undetected LAEs we make median stacked images for individual bandpasses. Since the vast majority (96%) are undetected in *K*, the spectral energy distributions (SEDs) constructed from stacking should closely represent the whole LAE population at each redshift. Since the time interval between the two redshifts is not so large (the age of the universe is $\simeq 2.0$ Gyr at $z = 3.1$ and $\simeq 1.7$ Gyr for $z = 3.7$), we treat the LAEs at $z = 3.1$ and 3.7 collectively as objects at $z \sim 3$, without discussing possible evolution between the two redshifts. In this paper, we show the results of our stellar population analysis of these LAEs. We also compare the stellar populations of LAEs with those of other high redshift galaxy populations. The contribution of LAEs to the cosmic star formation density and the stellar mass density is also evaluated.

The outline of this paper is as follows. In Section 2, we present our data and LAE sample. The SED fitting method is described in Section 3. In Section 4, we present and discuss our SED fitting results. A summary is given in Section 5. Throughout this paper, we use magnitudes in the AB system and assume a flat universe with $(\Omega_m, \Omega_\Lambda, h) = (0.3, 0.7, 0.7)$.

2 DATA

2.1 Optical and NIR Images

Deep *BVRi'z'* images of the SXDF were taken with Suprime-Cam on the Subaru Telescope by the Subaru/*XMM-Newton* Deep Survey project (SXDS; Furusawa et al. 2008). Ouchi et al. (2008) combined this public data set with their own imaging data taken with Suprime-Cam through two narrowband filters, *NB503* ($\lambda_c = 5029\text{\AA}$, $\Delta\lambda = 74\text{\AA}$) and *NB570* ($\lambda_c = 5703\text{\AA}$, $\Delta\lambda = 69\text{\AA}$), and constructed samples of 368 $z = 3.1$ and 116 $z = 3.7$ LAEs over a sky area of $\simeq 1 \text{ deg}^2$. These numbers are the logical sum of the spectroscopically-confirmed and photometrically-selected LAEs in Ouchi et al. (2008). They are selected as objects with narrow-band excesses and IGM absorption features shortward of Lyman α seen in color-color diagrams. The line-of-sight depth corresponding to the FWHM of the narrow-band filter is 55.7 comoving Mpc for NB503 and 43.2 comoving Mpc for NB570. For all LAEs, $2''$ -diameter aperture magnitudes were measured in each bandpass (Ouchi et al. 2008).

About 77% of the SXDF Suprime-Cam field was imaged in the *J*, *H*, and *K* bands with the wide-field near infrared camera WFCAM on the UKIRT in the UKIDSS/UDS project (Lawrence et al. 2007). The UKIDSS/UDS is underway, and we use Data Release 3 for this study. We align the *J*, *H*, *K* images with the SXDS optical images using common, bright stars, and then smooth them with Gaussian filters so that the PSF sizes of the *J*, *H*, *K* images match those of the optical images (FWHM $\approx 1.''0$). The 3σ limiting magnitudes over a $2''$ -diameter aperture are calculated to be $m_J = 24.5$, $m_H = 24.2$, and $m_K = 24.1$. Because the

¹ <http://ssc.spitzer.caltech.edu/legacy/abs/dunlop.html>

Table 1. Summary of Stellar Population Analysis of LAEs

Reference	Field	Area [arcmin ²]	redshift	N [†]	$m_{\text{threshold}}^{\ddagger}$ [mag]	Bands*	Remark
This Study	SXDF	2340	3.1	5(200)	$K(3\sigma) = 24.1$	$R, i, z, J, H, K, [3.6], [4.5], [5.8], [8.0]$	1
Gawiser et al. (2006)	ECDF-S	992	3.1	(18)	—	U, B, V, R, I, z, J, K	2
Gawiser et al. (2007)	ECDF-S	992	3.1	(52)	$[3.6](2\sigma) = 25.2$	$U, B, V, R, I, z, J, K, [3.6], [4.5], [5.8], [8.0]$	3
Lai et al. (2008)	ECDF-S	992	3.1	18(76)	$[3.6](2\sigma) = 25.2$	$B, V, R, I, z, [3.6], [4.5]$	4
Nilsson et al. (2007)	GOODS-S	44.4	3.15	(23)	$K_s(3\sigma) = 23.4$	$U, B, V, i, z', J, H, K_s, [3.6], [4.5], [5.8], [8.0]$	5
This Study	SXDF	2340	3.7	6(61)	$K(3\sigma) = 24.1$	$R, i, z, J, H, K, [3.6], [4.5], [5.8], [8.0]$	1
Pentericci et al. (2009)	GOODS-S	160	3.5 – 6	((38))	—	—	6
Finkelstein et al. (2009)	GOODS-S	160	4.0 – 5	11(3)	—	$NB, V, i', z', J, H, K, [3.6], [4.5]$	7
Pirzkal et al. (2007)	HUDF	11	4.00 – 5.76	5(4)	—	$z, J, H, K_s, [3.6], [4.5]$	8
Lai et al. (2007)	GOODS-N	160	5.7	3	$[3.6](3\sigma) = 26.2$	$i', z', [3.6], [4.5]$	9
Chary et al. (2005)	Abell 370	—	6.56	1	—	—	10

[†] Number of objects detected in at least one rest-frame optical band. The number in the parentheses is the number of objects not detected in any of the rest-frame optical bands.

[‡] Rest-frame optical detection threshold for LAEs, if given.

* Bands used for SED fitting, if given.

¹ K -detected objects are treated individually, while K -undetected objects are stacked.

² All objects are stacked.

³ All objects are stacked.

⁴ IRAC-detected and IRAC-undetected objects are stacked separately.

⁵ All objects are stacked.

⁶ LBGs with $\text{EW}(\text{Ly}\alpha) > 20 \text{ \AA}$, and all are treated individually irrespective of the NIR magnitude.

⁷ All objects are treated individually irrespective of the NIR magnitude.

⁸ All objects are treated individually irrespective of the NIR magnitude.

⁹ All objects are treated individually.

¹⁰ HCM 6A, a lensed LAE, detected at 3.6 and 4.5 μm . SED fitting is performed considering the effect of $\text{H}\alpha + [\text{NII}]$ emission in the 4.5 μm band.

zero-point magnitudes for the J, H, K images are given in the Vega system, we convert them into AB magnitudes using the offset values given in Table 7 of Hewett et al. (2006).

The SpUDS covers 0.65 deg² of the overlapping area of the SXDS and UDS fields (Figure 1). This 0.65 deg² area corresponds to an effective survey volume of $4.6 \times 10^5 \text{ Mpc}^3$ for $z = 3.1$ LAEs and $4.1 \times 10^5 \text{ Mpc}^3$ for $z = 3.7$ LAEs, respectively. All of the SpUDS IRAC images are geometrically matched to the optical images. We calculate the 3σ limiting magnitude over a $3''$ -diameter aperture to be $m_{3.6} = 24.8$, $m_{4.5} = 24.5$, $m_{5.8} = 22.7$, and $m_{8.0} = 22.6$ in the 3.6, 4.5, 5.8, and 8.0 μm IRAC bands, respectively.

2.2 Photometry

In this paper, we only analyse LAEs in the overlapping area of 0.65 deg² where the Suprime-Cam, WFCAM, and IRAC data (either channel 1+3 or 2+4) are all available. We perform $J, H,$ and K photometry with a $2''$ -diameter aperture at the position of LAEs in the narrowband images, using the IRAF task `apphot`.

We then convert $2''$ -diameter aperture magnitudes in the optical and JHK bands into total magnitudes in the following manner. First, we select 20 bright and isolated point sources in the R -band image, the deepest among all the images, and measure fluxes in a $2''$ aperture and in a series of larger apertures up to $5''$ with an interval of $0.1''$. Since we find the fluxes to level off for $> 4''$ apertures, we define $4''$ -aperture magnitudes as total magnitudes. Then, we select 100 point sources in the R -band image, measure fluxes over $2''$ and $4''$ apertures, and calculate an accurate offset between these two aperture magnitudes to be 0.17 mag. For each of the optical and JHK bandpasses, we sub-

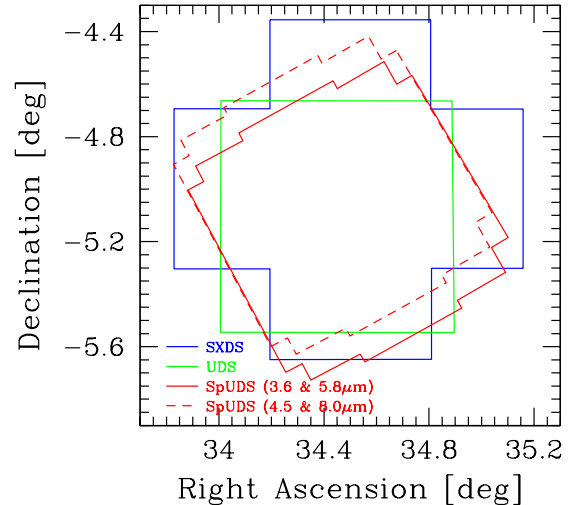


Figure 1. Observed field in the WCS coordinate system. The blue cross-shaped region is the SXDF imaged with Suprime-Cam. The green square corresponds to the UKIDSS/UDS (WFCAM) field. The red solid line and red dashed line outline the SpUDS fields with IRAC 3.6 μm and 5.8 μm imaging and 4.5 μm and 8.0 μm imaging, respectively.

tract 0.17 mag from $2''$ -aperture magnitudes to obtain total magnitudes for our LAEs.

For the Spitzer/IRAC four bands, we measure $3''$ -diameter aperture magnitudes for each LAE and converted them to total magnitudes by applying the aperture correc-

tion given by MUSYC survey². The correction values are 0.52, 0.55, 0.74, and 0.86 mag for $3.6\mu\text{m}$, $4.5\mu\text{m}$, $5.8\mu\text{m}$, and $8.0\mu\text{m}$, respectively.

2.3 The LAE samples used for the stellar population analysis

Table 2 summarises our LAE samples used for the stellar population analysis. Our original sample consists of 224 LAEs at $z = 3.1$ and 78 LAEs at $z = 3.7$, among which 35 and 21 have been spectroscopically confirmed, including two newly confirmed objects using Magellan/IMACS (Section 2.5).

We regard an object as LAE with AGN and exclude it from our analysis if it has a counterpart either in the XMM-Newton X-ray catalogue (Ueda et al. 2008) or in the VLA radio catalogue (Simpson et al. 2006), or its spectrum has emission lines typical of AGN, such as like SiIV, CIV, and HeII (for details, see Section 4.6 in Ouchi et al. 2008). It should be noted, however, that we cannot completely exclude contamination from X-ray-faint, radio-quiet, and/or heavily obscured AGNs.

In the stellar population analysis, we treat objects detected in the K band individually, while we stack K -undetected objects at each redshift to make an average SED and fit it with stellar population synthesis models. The K band corresponds to the rest-frame V and B bands for $z = 3.1$ and $z = 3.7$, respectively, both of which are redward of the 4000 \AA break. We find that the stacked objects of the two redshifts are both detected in K . Since as high as 96% of our sample are undetected in K (see below), the stacked SEDs of K -undetected objects is considered to represent closely the whole LAE population at the two redshifts.

2.4 K -detected LAEs

Among a total of 224 (78) LAEs at $z = 3.1$ (3.7), 9 (9) are found to be brighter than the K -band 3σ magnitude (i.e., 24.1 mag). Among these 18, 2 (1) objects at $z = 3.1$ (3.7) are found to host AGN (judged from the X-ray and radio data and spectroscopic data as described above), and 2 objects at $z = 3.7$ are found to be significantly confused by their neighbouring objects. we do not use them for the stellar population analysis. We then visually inspect the images of the remaining 13 K -bright objects, and find that one object is likely to be a false detection, because it is not detected in any of the other IR bands (J , H , and IRAC bands) and it falls on a low quality part of the K -band image. Next, we examine the SEDs of the remaining 12 objects over the range from the B band to the IRAC $8.0\mu\text{m}$ band, to find that one has an SED consistent with a late-type star, with a peak near the K band. After removal of these two objects, the number of LAEs brighter than $K(3\sigma)$ is five for $z = 3.1$ and six for $z = 3.7$. Hereafter, we call them " K -detected LAEs". Table 3 summarises their photometry, $L(\text{Ly}\alpha)$, $\text{EW}(\text{Ly}\alpha)$, and redshift.

We have found that the source center of NB503-N-21105 in the narrow band ($\text{Ly}\alpha$) offsets from those in the broad

bands (continuum) by about one arcsec. We thus cannot rule out the possibility that NB503-N-21105 is an LAE with a chance projection of a galaxy along the line-of-sight. However, the two components are more likely to be physically connected, because the narrow-band image is elongated to the direction of the offset.

NB570-N-32295 has a power-law like spectrum over the whole wavelength range up to $8.0\mu\text{m}$. Although we find that this spectrum is reproduced reasonably well by a stellar system (see Section 3.2), we cannot completely rule out a possible contamination from an AGN.

2.5 New Spectroscopy of Two Red Objects

Six out of the 11 K -detected LAEs have been spectroscopically identified by Ouchi et al. (2008) and Ouchi et al. in preparation. Among the remaining five, we selected two red objects, NB503-N-21105 and NB570-N-32295, and carried out spectroscopy with the Inamori Magellan Areal Camera and Spectrograph (IMACS) on the Magellan I Baade 6.5m telescope at the Las Campanas Observatory. The observation was made on 2008 December 19 with the WB4800 – 7800 filter and the 300 lines mm^{-1} grism whose blaze angle is 17.5 degrees. We chose a slit width of $1.0''$. The on-source exposure time was 15300 seconds under the $0.5'' - 0.75''$ seeing condition. The spectral coverage was $4800 - 7800 \text{ \AA}$. The spectral resolution and the corresponding velocity resolution are $R \simeq 890$ and $\Delta v \simeq 340 \text{ km s}^{-1}$ at 5029 \AA , and $\simeq 1000$ and 300 km s^{-1} at 5703 \AA . The data were reduced with the COSMOS pipeline version 2.12³.

We present the reduced 2D and 1D spectra in Figure 2. Both objects have a single, strong emission line ($> 6\sigma$ detection for NB503-N-21105 and $> 4\sigma$ detection for NB570-N-32295) and have no other emission line or detectable continuum emission⁴. The central wavelength of the single line is 5035.4 \AA for NB503-N-21105, and 5693.9 \AA for NB570-N-32295. We conclude that both objects are a real LAE from the following discussion. If NB503-N-21105 is an [O III] ([O II]) emitter, $\text{H}\alpha$ ([O III]) emission should be detected at $\simeq 6629 \text{ \AA}$ (6759 \AA). Similarly, if NB570-N-32295 is an [O III] ([O II]) emitter, $\text{H}\alpha$ ([O III]) emission should be seen at $\simeq 7482 \text{ \AA}$ (7661 \AA). We summarise the spectroscopic results in Table 4.

2.6 Stacking of K -undetected LAEs

Among the LAEs fainter than the $K(3\sigma)$ magnitude, 200 (61) at $z = 3.1$ (3.7) have all 10 broadband data from R to $8.0\mu\text{m}$ and do not show AGN features, to be used for the stellar population analysis. We call these LAEs " K -undetected LAEs". We make median-stacked multi-waveband images separately for the two redshifts. Table 5 summarises their photometry, average $L(\text{Ly}\alpha)$, $\text{EW}(\text{Ly}\alpha)$

³ <http://www.ociw.edu/Code/cosmos>

⁴ There is an emission-like feature around [C IV] in the spectrum of NB570-N-32295. We find, however, that there is a strong sky emission line at this wavelength and that this feature is statistically insignificant, being consistent with a residual of sky subtraction.

² http://www.astro.yale.edu/dokkum/SIMPLE/release_1.1/doc/OOREADME-photometry

Table 2. Summary of our samples used for the stellar population analysis

LAE sample	<i>K</i> -band detection	<i>N</i>	with spec- <i>z</i>	referred to as
<i>z</i> = 3.1				
Total	–	224	35	–
LAE without AGN	Yes	5	5	<i>K</i> -detected LAEs
LAE with AGN	Yes	2	2	–
noise (false detection)	Yes	1	0	–
late-type star	Yes	1	0	–
LAE in the SpUDS files and without AGN	No	200	27	<i>K</i> -undetected LAEs
LAE out of the SpUDS files and/or with AGN	No	15	1	–
<i>z</i> = 3.7				
Total	–	78	21	–
LAE without AGN	Yes	6	3	<i>K</i> -detected LAEs
LAE with AGN	Yes	1	1	–
confusion	Yes	2	2	–
LAE in the SpUDS files and without AGN	No	61	14	<i>K</i> -undetected LAEs
LAE out of the SpUDS files and/or with AGN	No	8	1	–

Table 3. *K*-detected LAE sample

Object Name	<i>R</i>	<i>i'</i>	<i>z'</i>	<i>J</i>	<i>H</i>	<i>K</i>	3.6 μ m	4.5 μ m	5.8 μ m	8.0 μ m	log <i>L</i> (Ly α) [erg s ⁻¹]	EW(Ly α) [Å]	<i>z</i>	Ref.
NB503-N-21105 (R1)	26.2	25.9	26.0	24.3	23.6	23.9	22.4	22.5	22.8 [†]	22.9 [†]	42.49	73	3.142	(1)
NB503-N-42377	23.8	23.8	23.9	23.8	23.8 [†]	23.0	23.7	24.2 [†]	23.1 [†]	22.3 [†]	43.50	77	3.154	(2)
NB503-S-45244	24.6	24.6	24.8	99.9 [†]	25.1 [†]	23.6	24.7 [†]	–	99.9 [†]	–	43.21	86	3.156	(2)
NB503-S-65716	23.9	23.9	24.1	24.3	23.8	23.5	24.1	–	99.9 [†]	–	43.38	65	3.114	(3)
NB503-S-94275	24.3	24.3	24.5	24.5 [†]	24.8 [†]	23.6	24.9 [†]	24.4 [†]	99.9 [†]	23.7 [†]	43.56	147	3.102	(2)
NB570-N-32295 (R2)	27.1	26.5	26.2	25.3 [†]	24.6 [†]	23.5	22.6	22.3	21.6	21.5	42.74	225	3.684	(1)
NB570-S-84321	24.9	24.8	25.0	24.4 [†]	24.0	23.7	24.3 [†]	23.7	26.7 [†]	24.2 [†]	42.99	55	3.648	(2)
NB570-W-55371	24.6	24.6	24.6	25.3 [†]	24.1 [†]	23.3	23.8	23.9	23.2 [†]	99.9 [†]	42.71	20	3.699	(2)
NB570-C-24119	25.5	25.2	25.1	26.8 [†]	24.7 [†]	23.2	23.0	22.5	22.0 [†]	22.0 [†]	42.58	34	3.69*	
NB570-S-88963 (R3)	26.1	25.4	25.4	24.2	25.2 [†]	23.2	23.1	22.6	22.8 [†]	22.8 [†]	42.83	106	3.69*	
NB570-W-59558 (R4)	25.7	25.4	25.2	24.2	24.0	23.0	23.3	23.1	99.9 [†]	23.8 [†]	43.12	150	3.69*	

NOTES: All magnitudes are total magnitudes. No value means that the object is out of the image.

Negative fluxes have been replaced with 99.9 mag. Sources of spectroscopic redshifts are (1) this study, (2) Ouchi et al. (2008), (3) Ouchi et al. in preparation.

[†]Fainter than the 3 σ limiting magnitude.

*Not spectroscopically confirmed. we give *z* = 3.69, which corresponds to the central wavelength of NB570.

Table 4. Spectroscopic results of two red LAEs

Object Name	RA (J2000) [h:m:s]	Dec (J2000) [d:m:s]	FWHM(Ly α) [†] [km s ⁻¹]	<i>z</i>
NB503-N-21105 (R1)	2:18:42.186	−4:46:38.54	205 ± 129	3.142
NB570-N-32295 (R2)	2:17:25.630	−4:44:33.57	629 ± 201	3.684

[†]After correction for the instrumental broadening on the assumption of a Gaussian profile.

Table 5. Stacked median LAE sample.

Object Name	<i>R</i>	<i>i'</i>	<i>z'</i>	<i>J</i>	<i>H</i>	<i>K</i>	3.6 μ m	4.5 μ m	5.8 μ m	8.0 μ m	log <i>L</i> (Ly α) [erg s ⁻¹]	EW(Ly α) [Å]	(<i>z</i>)
NB503- <i>K</i> -undetected	26.9	26.9	27.1	27.4 [†]	28.8 [†]	26.5	27.1	27.4 [†]	99.9 [†]	99.9 [†]	42.54	155	3.14*
NB570- <i>K</i> -undetected	26.4	26.3	26.4	26.9 [†]	27.2 [†]	25.4	26.5	29.2 [†]	25.5 [†]	99.9 [†]	42.82	135	3.69*

NOTES: All magnitudes are total magnitudes. Negative fluxes have been replaced with 99.9 mag.

[†]Fainter than the 3 σ limiting magnitude.

*Redshifts corresponding to the central wavelengths of NB503 and NB570.

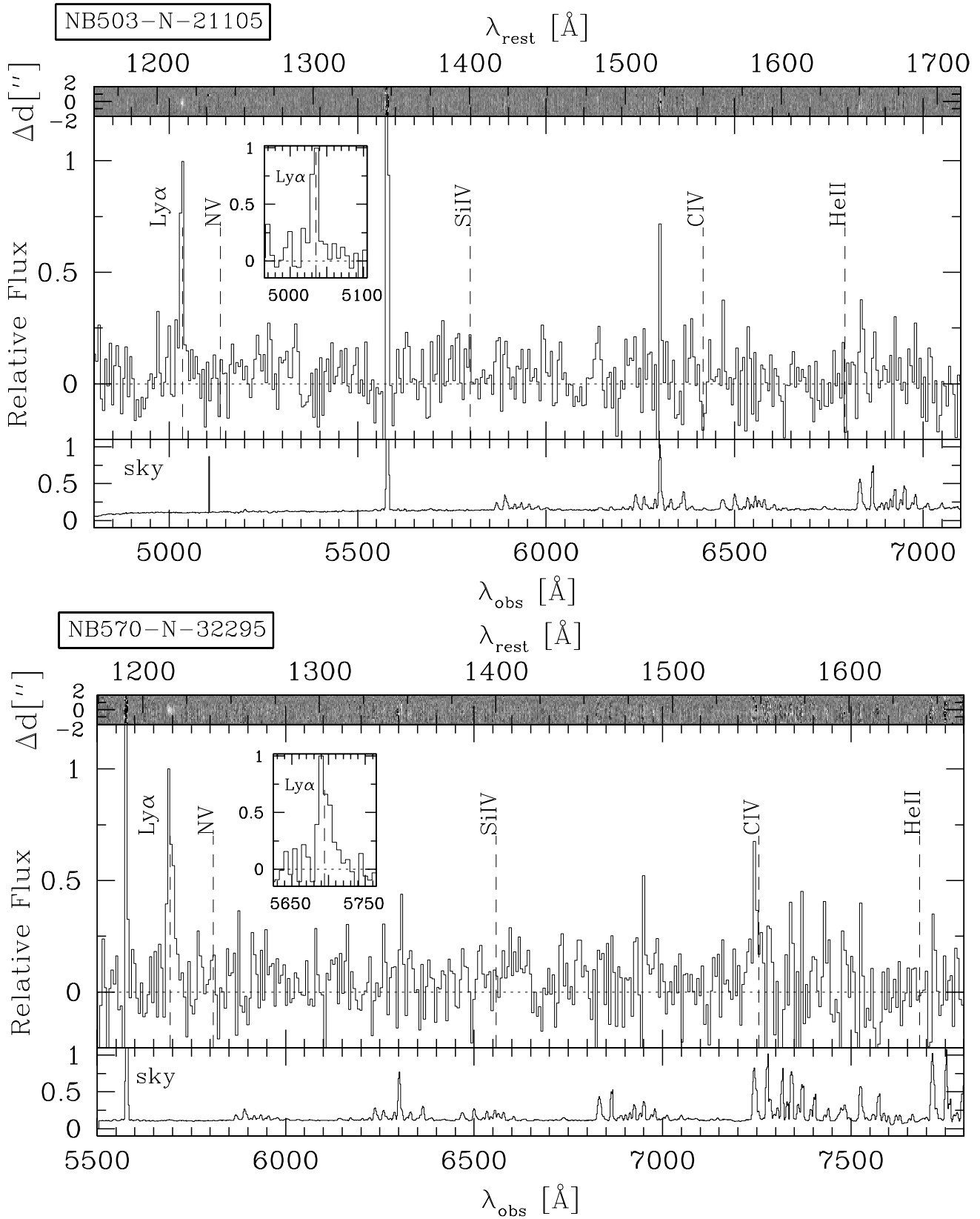


Figure 2. Spectra of NB503-N-21105 (top) and NB570-N-32295 (bottom). For each object, the top and middle panels show the two- and one-dimensional spectra, respectively. The one-dimensional spectra have been smoothed with a 3 pixel boxcar. The dashed lines with the legend correspond to the wavelengths of typical emission lines from AGN. Inserted is a zoom up around Ly α line. The bottom panel shows the sky background with an arbitrary normalisation.

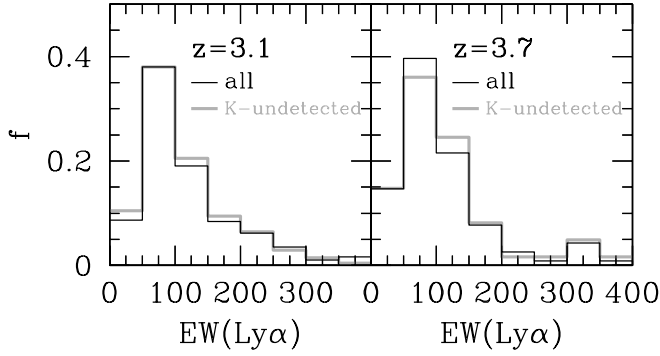


Figure 3. Normalised histograms of the rest-frame Ly α EWs for all (black) and K -undetected (grey) LAEs at $z = 3.1$ (left) and 3.7 (right).

derived from narrow-band and R -band magnitudes, and redshift. In Figure 3, we show the histograms of the rest-frame Ly α EWs for all and K -undetected LAEs, to confirm that the K -undetected LAEs are representative of the whole sample.

2.7 Applications of Broadband Color Selections

2.7.1 LBG Selection

We examine whether the six K -detected LAEs at $z = 3.7$ are selected as LBGs, by applying the BRi' colour selection criteria for $z \sim 4$ LBGs (e.g. Ouchi et al. 2004; Yoshida et al. 2006). None of them are found to meet the criteria. This is probably because our objects tend to have redder UV slopes than typical LBGs, or the B -band image is not deep enough to detect Lyman break, or the redshift of $z = 3.7$ is close to the edge of the redshift range covered by the BRi' selection criteria.

In addition, we apply the BRi' colour criteria to the 61 K -undetected LAEs at $z = 3.7$ and find that only seven satisfy the criteria. We also find that the stacked LAE at $z = 3.7$ does not meet the criteria.

2.7.2 DRG Selection

We then apply the colour criterion for distant-red galaxies (DRGs), $J - K > 1.3$, to our sample, and find that none of the K -detected LAEs and the two stacked LAEs satisfies the DRG criterion. We also apply the colour criterion to the best-fit model SEDs for these LAEs derived from our SED fitting (Section 3). Among the 11 K -detected LAEs, model SEDs for three (NB503-N-21105, NB570-N-32295, and NB570-C-24119) meet the criterion. The former two have very red SEDs and have very large dust extinction ($E(B - V)_* \sim 0.65$). We will focus on this kind of LAEs in Section 4.2.

3 SED FITTING

3.1 Method

After obtaining rest-frame UV-to-optical photometry for the K -detected and stacked LAEs, we analyse their stel-

lar populations by the standard SED fitting method (e.g., Furusawa et al. 2000; Papovich et al. 2001). We use the stellar population synthesis model of GALAXEV (Bruzual & Charlot 2003, hereafter BC03) to produce model SEDs. Most of the previous studies have used BC03 (Table 6). We make a large set of mass-normalised model SEDs, varying star-formation timescale, age, and dust extinction (or $E(B - V)_*$). These SEDs are then redshifted to $z = 3.1$ and $z = 3.7$ and convolved with ten bandpasses, R, i, z, J, H, K , and IRAC four bands, to calculate flux densities. For each LAE, we search for the best-fit SED that minimizes

$$\chi^2 = \sum_i \frac{[f_{\text{obj}}^{(i)} - M_{\text{star}} f_{\text{model}}^{(i)}(\text{age}, E(B - V)_*, \tau)]^2}{\sigma^2(f_{\text{obj}}^{(i)})}, \quad (1)$$

where $f_{\text{obj}}^{(i)}$ is the observed flux density in the i -th bandpass, $f_{\text{model}}^{(i)}$ is the mass-normalised model flux density in the i -th bandpass, τ is the star-formation timescale, and $\sigma(f_{\text{obj}}^{(i)})$ is the photometric error in the i -th bandpass. Because M_{star} is the amplitude of a model SED, we obtain the best-fit M_{star} for each set of (age, $E(B - V)_*$, τ) by solving $\partial\chi^2/\partial M_{\text{star}} = 0$, and calculate χ^2 . Then we search for the set of the best-fit parameters that gives the minimum χ^2 . The errors in the best-fit SED parameters correspond to 1σ confidence interval ($\Delta\chi^2 < 1$) for each parameter.

We do not use either B - or V -band photometry in the fitting, since B -band photometry suffers from the IGM absorption shortward of the Lyman α wavelength and V -band photometry is contaminated from Ly α emission. The amount of the IGM absorption considerably differs by the line of sight. Ly α fluxes can be estimated from narrow and broad band photometry, but they have an uncertainty of a factor of ~ 2 (see Figure 15 of Ouchi et al. 2008). The shortest broadband we use for SED fitting is the R band, which corresponds to 1585 Å and 1380 Å for $z = 3.1$ and 3.7 LAEs. These wavelengths are very close to Ly α and short enough to cover the wide range of SEDs.

We adopt Salpeter's initial mass function (Salpeter 1955) with lower and upper mass cutoffs of 0.1 and $100M_{\odot}$. We fix the metallicity to $Z/Z_{\odot} = 0.2$, considering the fact that LBGs at $z \sim 3$ tend to have subsolar metallicities at $Z/Z_{\odot} \sim (1/4) - (1/3)$ (a strongly lensed LBG, cB58: Pettini et al. 2000; Teplitz et al. 2000) and $Z/Z_{\odot} \sim (1/10) - (2/3)$ (four bright LBGs: Pettini et al. 2001). Although Shapley et al. (2004) reported that very massive $z \sim 2$ LBGs with $M_{\text{star}} \sim 10^{11}M_{\odot}$ have approximately the solar metallicity, Erb et al. (2006) found that less massive ($\lesssim 10^{10}M_{\odot}$) LBGs at similar redshifts have subsolar metallicities (see also, Maiolino et al. 2008). It appears to be reasonable that the metallicities of typical LAEs are lower than (and at most comparable to) those of typical LBGs.

We also examine models with $Z/Z_{\odot} = 0.005$ and 1, and find that while the best-fit stellar mass is insensitive to metallicity over this range, the best-fit age and dust extinction become higher with decreasing metallicity. However, the dependencies of age and dust extinction on metallicity are not so strong: for both parameters, the change from the best-fit value for the $Z/Z_{\odot} = 0.02$ model is within its 1σ errors.

Table 6. Summary of Stellar Population Analysis of LAEs: Assumption on SED Modeling

Reference	Model [†]	IMF	SFH [‡]	Metallicity [Z_{\odot}]	Extinction* Curve	Remarks
This Study	BC03, CB08	Salpeter	const, exp	0.005, 0.02, 0.2, 1	C00	(O09)
Gawiser et al. (2006)	BC03	Salpeter	const	1	C97	
Gawiser et al. (2007)	M05	Salpeter	two-burst	0.02 – 1	C00	
Lai et al. (2008)	BC03	Salpeter	const	1	C00	
Nilsson et al. (2007)	BC03	Salpeter	const	0.005, 0.2, 1	CF00	
Pentericci et al. (2009)	BC03, M05, CB08	Salpeter	exp	0.02, 0.2, 1, 2.5	C00	(P09)
Finkelstein et al. (2009)	BC03	Salpeter	exp, two bursts	0.005, 0.02, 0.2, 0.4, 1	C94	(F09)
Pirzkal et al. (2007)	BC03	Salpeter	ssp, exp, 2bp	0.005 – 2.5	C00	
Lai et al. (2007)	BC03	Salpeter	ssp, const	0.005, 1	C00	
Chary et al. (2005)	BC03	Salpeter	—	0.02	—	

[†] Population synthesis model. "BC03", "M05", and "CB08" represent Bruzual & Charlot (2003), Maraston (2005), and the unpublished Charlot & Bruzual model, respectively.

[‡] Star formation history. "ssp": instantaneous starburst, "const": constant star formation history, "exp": exponentially decaying star formation history (and τ is e -folding time), "two-burst": superposition of an old instantaneous burst component and a young "exp" component, "two bursts": superposition of an old "exp" component (age = 1.4 Gyr and $\tau = 10^5$ yr) and a young "exp" component ($\tau = 10^5$ yr), "2bp": superposition of two different instantaneous starbursts. The e -folding times examined are: $\tau = 1, 10, 10^2, 10^3$ Myr (**O09**), $\tau = 0.1, 0.3, 0.6, 1, 1.5, 2, 3, 4, 5, 7, 9, 13, 15$ Gyr (**P09**), $\tau = 10^5, 10^6, 10^7, 10^8, 4 \times 10^9$ yr (**F09**).

* Dust extinction law. C00: Calzetti et al. (2000), C97: Calzetti et al. (1997), C94: Calzetti et al. (1994), CF00: Charlot&Fall (2000).

The star formation timescales examined are (i) constant star formation and (ii) exponentially decaying star formation with four e -folding times of $\tau = 0.001, 0.01, 0.1, 1$ Gyr, and we search for the best-fit SED separately for the cases (i) and (ii). As explained in the next section, we adopt the results for constant star formation for our discussion of stellar populations. For dust extinction, we use Calzetti's extinction law (Calzetti et al. 2000) and vary $E(B - V)_*$ over 0 and 1.50 with an interval of 0.01.

Models of constant star formation have three free parameters, stellar mass, age, and dust extinction, while models of exponentially decaying star formation have one more parameter, e -folding time.

3.2 Results

Figures 4 and 5 show the results of the SED fitting for objects at $z = 3.1$ and 3.7 . For each object, the blue and red curves correspond respectively to the best-fit SEDs for constant star formation and for exponentially decaying star formation. Both SEDs give similarly good fits for most of the objects, implying a difficulty in constraining the star formation history.

The best-fit parameters are summarised in Table 7 for constant star formation and Table 8 for exponentially decaying star formation. The reduced χ^2 tends to be slightly larger for the model of exponentially decaying star formation. This may be because the e -folding time interval adopted is too large (1 dex) to fine-tune model SEDs. In any case, adding the e -folding time as a free parameter does not significantly improve the fit.

It is found from these tables that the two models give very similar stellar masses, and thus that the stellar mass is a robust parameter against the assumed star formation history. Dust extinction is also relatively insensitive to the star formation history. The only exception is NB570-W-59558, for which $E(B - V)_* = 0.63$ for constant star formation and 0.00 for exponentially decaying star formation.

On the other hand, age and SFR largely differ between the two models for some objects. The ages of two objects (NB570-C-24119 and NB570-W-59558) differ by more than one order of magnitude, and the SFRs of seven objects (NB503-S-65716, NB503-S-94275, NB503-N-21105, NB503-K-undetected, NB570-C-24119, NB570-N-32295, NB570-W-59558) differ by more than one order of magnitude. All but one of these seven objects have $\tau = 0.001$ Gyr, i.e., burst-like star formation histories. In other words, these objects are equally well fitted by two extremes, constant star formation and burst-like star formation, and our data cannot discriminate between them. It will be resolved by deeper NIR imaging (e.g., Pozzetti & Mannucci 2000) and/or other independent observations such as submillimetre imaging.

In the following discussion, we will adopt the results for constant star formation, because (i) the values of reduced χ^2 are lower for constant star formation for all but one object and (ii) it is easy to compare our results with previous SED studies on LAEs since most of them have also adopted constant star formation.

Most of the LAEs have a brighter K -band magnitude than the best-fit SED. The reason for this discrepancy is not clear, but a possible reason is that the K -band flux density is affected by [O III] and $H\beta$ emission. On the basis of the relations between SFR and [O III] and $H\beta$ emission strengths (Kennicutt 1998; Moustakas et al. 2006), we find that these lines may significantly increase K -band flux densities if SFR is higher than $\sim 10^3 [M_{\odot} \text{ yr}^{-1}]$. However, since most of the objects have $\text{SFR} \lesssim 10^3 M_{\odot} \text{ yr}^{-1}$, this effect cannot explain the observed excesses. Another possible reason is that a relatively faint magnitude, $K(3\sigma) = 24.1$, is adopted for the boundary of K -detection. Our K -detected sample may include objects whose K magnitude happens to be brighter than the true value due to positive sky noise at the position of the objects. However, most of the K -detected objects are also detected in at least one of the J, H , and the four IRAC bands, suggesting that they are truly bright in the near-infrared wavelengths and thus that the systematic

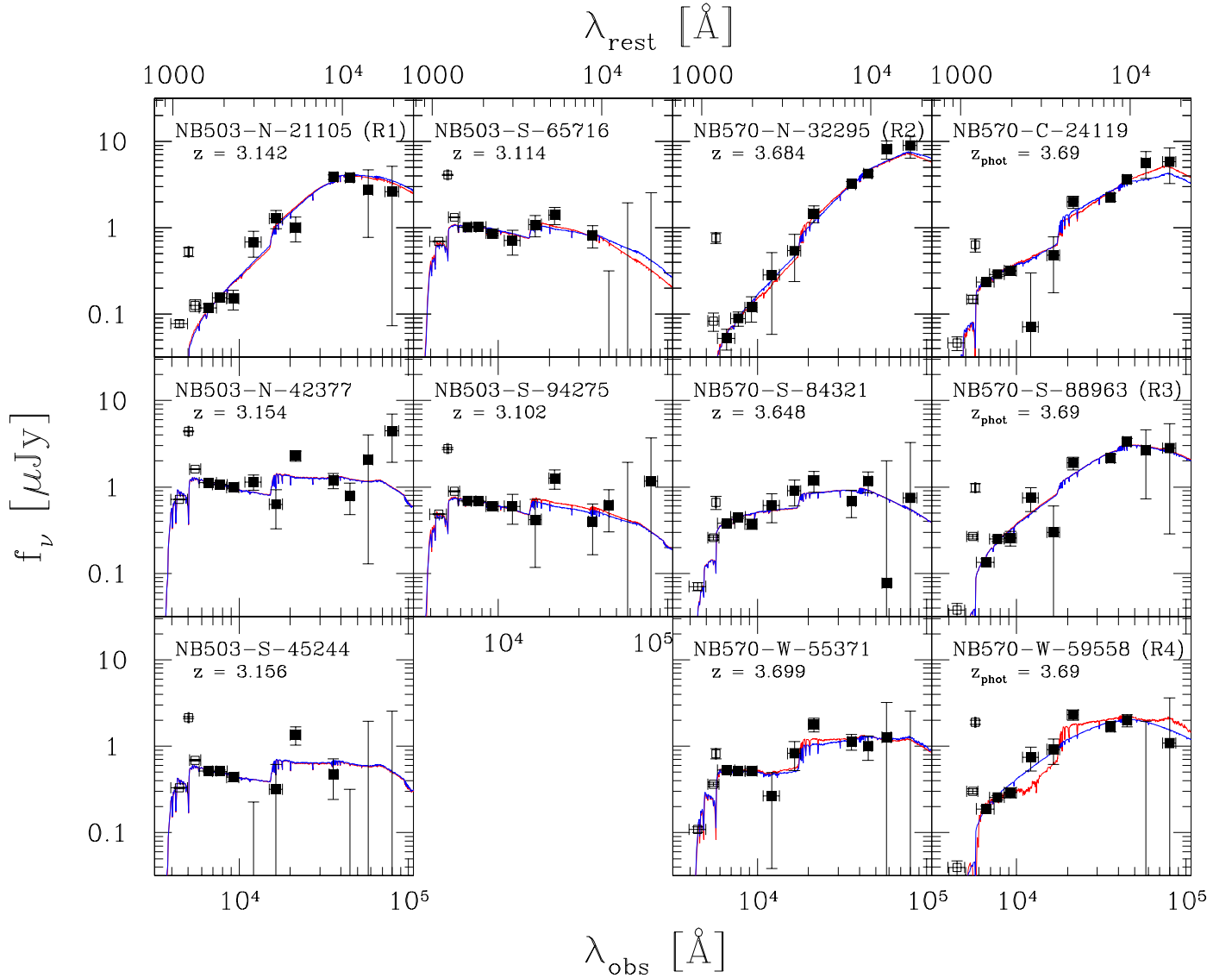


Figure 4. Best-fit model SEDs (curves) and observed photometry (squares) for K -detected LAEs. The blue and red curves correspond to constant star formation and exponentially decaying star formation, respectively. Data shown by open squares are not used for the SED fitting.

brightening of K is not very strong. We infer that the systematic brightening of K , if any, does not significantly affect the best-fit SEDs which are determined from the overall shapes of observed SEDs from R to IRAC $8.0\mu\text{m}$ bands. Indeed, we perform the SED fitting excluding K photometry, and find that for any object the best-fit parameters which are different from the original values only within the 1σ errors, although the best-fit stellar masses tend to be slightly (≈ 0.05 dex) smaller.

Most of the errors in the best-fit parameters of NB503- K -undetected are larger than those of NB570- K -undetected in spite of a larger number of objects being stacked in NB503. This is because NB503- K -undetected is fainter in most bandpasses as shown in Table 5. The $z = 3.1$ LAE sample includes fainter objects than the $z = 3.7$ sample since the limiting magnitude in NB503 is fainter by 0.6 mag (see Section 2.2 in Ouchi et al. 2008). Thus, the K -undetected ob-

jects in the $z = 3.1$ sample are on average fainter than those in the $z = 3.7$ sample. We also note that the reduced χ^2 is smaller for NB503- K -undetected. We infer that this is not only because the observed K -band flux density for NB570- K -undetected is much brighter than the best-fit SED (see Figure 5), but also because the magnitude errors of NB503- K -undetected are larger.

Some new population synthesis models include thermally pulsating asymptotic giant branch (TP-AGB) stars (e.g., Maraston 2005; Bruzual 2007). Inclusion of TP-AGB stars should have little effect on the SED fitting for most LAEs, because LAEs are in general very young and have subsolar metallicities (e.g., Pentericci et al. 2009; Gawiser 2009). In our sample, however, four objects (NB503-N-42377, NB503-S-45244, NB570-W-55371, and NB570-C-24119) have relatively old ages of > 300 Myr and thus their NIR fluxes could be dominated by TP-AGB stars. We fit

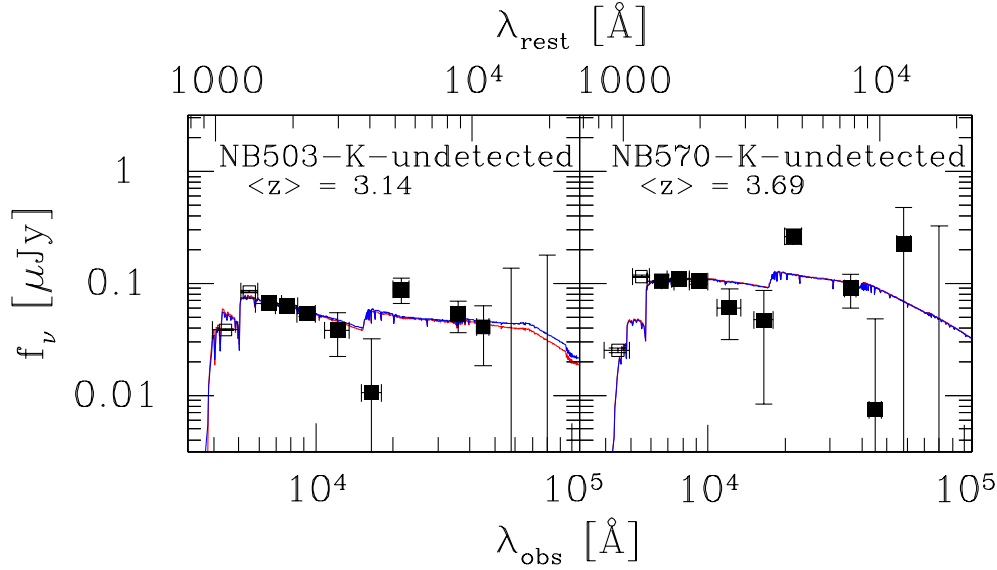


Figure 5. Same as Figure 4, but for K -undetected (stacked) LAEs.

Table 7. SED Fitting Result ($Z = 0.2Z_{\odot}$, constant SFH)

Object Name	$\log M_{\text{star}}$ [M_{\odot}]	$E(B - V)_{\star}$ [mag]	$\log(\text{Age})$ [yr]	$\log(\text{SFR})$ [$M_{\odot} \text{ yr}^{-1}$]	χ_r^2 *
$z = 3.1$					
NB503-N-21105 (R1)	$10.43^{+0.22}_{-0.13}$	$0.70^{+0.05}_{-0.05}$	$6.68^{+0.28}_{-0.12}$	$3.75^{+0.34}_{-0.40}$	2.36
NB503-N-42377	$9.82^{+0.09}_{-0.10}$	$0.00^{+0.02}_{-0.00}$	$8.51^{+0.10}_{-0.20}$	$1.40^{+0.09}_{-0.01}$	2.75
NB503-S-45244	$9.58^{+0.23}_{-0.34}$	$0.00^{+0.07}_{-0.00}$	$8.61^{+0.25}_{-0.70}$	$1.06^{+0.35}_{-0.01}$	2.17
NB503-S-65716	$9.19^{+0.13}_{-0.08}$	$0.13^{+0.05}_{-0.03}$	$6.98^{+0.40}_{-0.34}$	$2.22^{+0.46}_{-0.26}$	1.91
NB503-S-94275	$8.97^{+0.58}_{-0.13}$	$0.11^{+0.07}_{-0.11}$	$7.10^{+1.26}_{-0.48}$	$1.88^{+0.59}_{-0.68}$	0.96
NB503- K -undetected	$8.12^{+0.26}_{-0.37}$	$0.03^{+0.05}_{-0.03}$	$7.81^{+0.45}_{-0.81}$	$0.36^{+0.44}_{-0.17}$	1.39
$z = 3.7$					
NB570-N-32295 (R2)	$10.60^{+0.54}_{-0.11}$	$0.67^{+0.04}_{-0.25}$	$7.40^{+1.81}_{-0.38}$	$3.23^{+0.27}_{-1.19}$	0.57
NB570-S-84321	$9.59^{+0.23}_{-0.16}$	$0.32^{+0.05}_{-0.08}$	$6.68^{+0.85}_{-0.12}$	$2.91^{+0.35}_{-0.73}$	1.34
NB570-W-55371	$10.19^{+0.10}_{-0.17}$	$0.04^{+0.04}_{-0.04}$	$8.96^{+0.25}_{-0.35}$	$1.33^{+0.19}_{-0.15}$	1.15
NB570-C-24119	$10.67^{+0.17}_{-0.15}$	$0.29^{+0.07}_{-0.08}$	$8.71^{+0.50}_{-0.50}$	$2.06^{+0.33}_{-0.33}$	1.39
NB570-S-88963 (R3)	$10.54^{+0.29}_{-0.33}$	$0.62^{+0.06}_{-0.10}$	$6.56^{+0.44}_{-0.74}$	$3.98^{+0.37}_{-0.75}$	1.93
NB570-W-59558 (R4)	$10.71^{+0.03}_{-0.69}$	$0.63^{+0.01}_{-0.16}$	$6.16^{+0.74}_{-1.06}$	$4.55^{+1.09}_{-1.42}$	2.14
NB570- K -undetected	$8.50^{+0.20}_{-0.10}$	$0.19^{+0.04}_{-0.03}$	$6.76^{+0.16}_{-0.22}$	$1.74^{+0.42}_{-0.22}$	3.27

*Reduced χ squares. The degree of freedom is 5 ($= 8 - 3$) for NB503-S-45244 and NB503-S-65716, and 7 ($= 10 - 3$) for the others.

a new version of GALAXEV which includes TP-AGB stars (Charlot & Bruzual, in preparation) to these four, and obtain almost the same results as for BC03, except decreases in stellar mass of 0.2 – 0.3 dex.

4 RESULTS AND DISCUSSION

Figure 6 shows the distributions of the best-fit parameters derived from the SED fitting. The stellar masses of the K -detected LAEs are distributed over $M_{\text{star}} \sim 10^9 - 10^{10.5} M_{\odot}$, while those of the K -undetected LAEs are much less massive ($M_{\text{star}} \sim 10^8 - 10^{8.5} M_{\odot}$). The K -detected LAEs have a large

variety of dust extinction with $0 < E(B - V)_{\star} < 0.7$, while the K -undetected LAEs have mild dust extinction. The ages of our LAEs are distributed over around $10^6 - 10^9$ yr. The age distribution of the K -detected objects could be bimodal, although its statistical significance is low. The ages of the K -undetected LAEs are around the median of the K -detected LAEs. The SFRs of the K -detected LAEs span a wide range of $10 - 10^4 M_{\odot} \text{ yr}^{-1}$, while those of the K -undetected LAEs are between $1 - 100 M_{\odot} \text{ yr}^{-1}$.

The $E(B - V)_{\star}$ of NB570- K -undetected is significantly larger than that of NB503- K -undetected. This may merely reflect the fact that NB570- K -undetected is more massive

Table 8. SED Fitting Result ($Z = 0.2Z_{\odot}$, exponentially decaying SFH)

Object Name	$\log M_{\text{star}}$ [M_{\odot}]	$E(B - V)_{\star}$ [mag]	$\log(\text{Age})$ [yr]	$\log(\text{SFR})$ [$M_{\odot} \text{ yr}^{-1}$]	e-folding time [Gyr]	χ_r^2 *
$z = 3.1$						
NB503-N-21105 (R1)	$10.13^{+0.51}_{-0.02}$	$0.64^{+0.11}_{-0.33}$	$6.64^{+1.52}_{-0.12}$	$2.24^{+1.79}_{-\infty}$	0.001	2.71
NB503-N-42377	$9.82^{+0.05}_{-0.12}$	$0.00^{+0.02}_{-0.00}$	$8.46^{+0.05}_{-0.35}$	$1.38^{+0.09}_{-0.10}$	1	3.21
NB503-S-45244	$9.54^{+0.21}_{-0.81}$	$0.00^{+0.07}_{-0.00}$	$8.51^{+0.20}_{-1.57}$	$1.05^{+0.36}_{-2.54}$	1	2.72
NB503-S-65716	$8.99^{+0.12}_{-0.04}$	$0.11^{+0.03}_{-0.04}$	$6.66^{+0.26}_{-0.04}$	$1.01^{+0.26}_{-1.53}$	0.001	2.10
NB503-S-94275	$8.87^{+0.62}_{-0.19}$	$0.06^{+0.10}_{-0.05}$	$6.92^{+1.29}_{-0.38}$	$-0.73^{+3.11}_{-1.66}$	0.001	1.05
NB503-K-undetected	$7.75^{+0.61}_{-0.12}$	$0.01^{+0.05}_{-0.01}$	$7.00^{+1.21}_{-0.10}$	$-2.57^{+3.10}_{-0.80}$	0.001	1.56
$z = 3.7$						
NB570-N-32295 (R2)	$10.84^{+0.14}_{-0.37}$	$0.48^{+0.22}_{-0.05}$	$7.81^{+0.85}_{-0.73}$	$-22.91^{+26.29}_{-\infty}$	0.001	0.56
NB570-S-84321	$9.54^{+0.42}_{-0.30}$	$0.31^{+0.06}_{-0.03}$	$6.68^{+1.33}_{-0.16}$	$2.75^{+0.51}_{-\infty}$	0.01	1.55
NB570-W-55371	$10.05^{+0.04}_{-0.07}$	$0.00^{+0.03}_{-0.00}$	$8.46^{+0.00}_{-0.05}$	$0.93^{+0.14}_{-0.00}$	0.1	1.08
NB570-C-24119	$10.39^{+0.37}_{-0.07}$	$0.29^{+0.05}_{-0.06}$	$7.60^{+1.30}_{-0.16}$	$-12.92^{+15.17}_{-6.41}$	0.001	1.53
NB570-S-88963 (R3)	$10.54^{+0.25}_{-0.39}$	$0.63^{+0.05}_{-0.10}$	$6.50^{+0.44}_{-0.04}$	$3.18^{+1.09}_{-0.76}$	0.001	2.23
NB570-W-59558 (R4)	$10.46^{+0.02}_{-0.08}$	$0.00^{+0.01}_{-0.00}$	$8.56^{+0.00}_{-0.05}$	$-12.08^{+1.65}_{-\infty}$	0.01	1.85
NB570-K-undetected	$8.49^{+0.20}_{-0.26}$	$0.19^{+0.04}_{-0.06}$	$6.74^{+0.18}_{-0.22}$	$1.74^{+0.41}_{-2.29}$	0.1	3.82

*Reduced χ squares. The degree of freedom is 4 ($= 8 - 4$) for NB503-S-45244 and NB503-S-65716, and 6 ($= 10 - 4$) for the others.

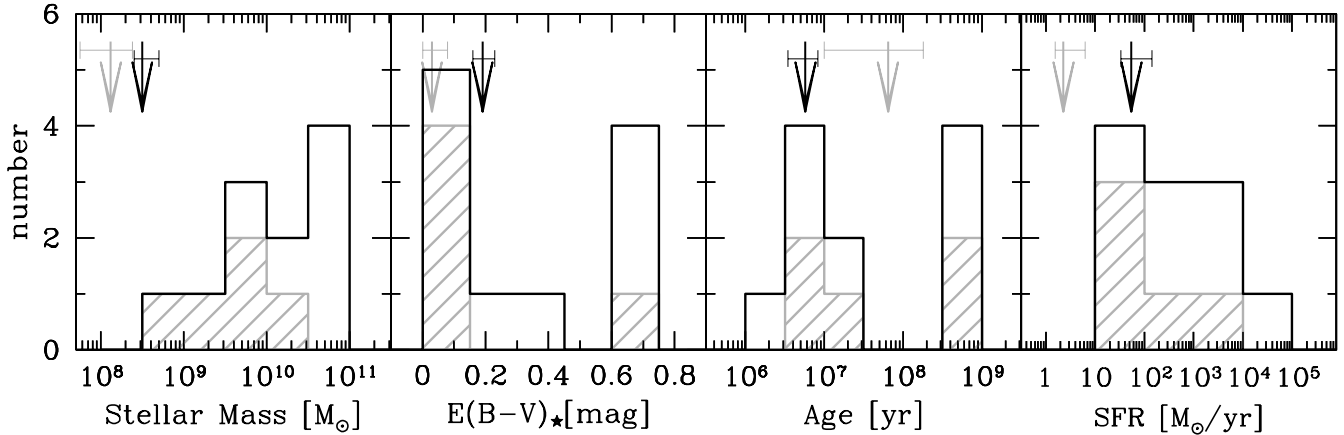


Figure 6. Distributions of the best-fit parameters derived from the SED fitting. The shaded histograms are for the K -detected LAEs at $z = 3.1$, and the open histograms are for the sum of the K -detected LAEs at $z = 3.1$ and 3.7 . Grey and black arrows indicate the K -undetected LAEs at $z = 3.1$ and 3.7 , respectively.

and thus has produced more metal. On the other hand, this could reflect some evolution of the LAE population between the two redshifts. Indeed, it is found in Table 9 that LAEs at $z > 3.7$ can have $E(B - V)_{\star}$ comparable to or larger than that of NB570- K -undetected.

We find that four objects have extremely large extinction $E(B - V)_{\star} \sim 0.65$: NB503-N-21105, NB570-N-32295, NB570-S-88963, and NB570-W-59558⁵. Their prop-

⁵ This object is equally well fitted by two extremes: a young and dusty starburst galaxy with constant SFH, and an old and dead galaxy with exponentially decaying SFH. This is caused by the age-dust degeneracy. Although our data cannot discriminate between them, we treat this object as a young and dusty starburst galaxy in this section (see details in Section 3.2)

erties (other than age) are clearly different from the other LAEs, as we can see in the following subsections. We label the four objects as R1 – R4 in most of the forthcoming figures. These four red LAEs may be a distinct population, and we will discuss this in Section 4.2.

4.1 Correlations among Stellar Population Parameters

Table 9 summarises the results of the stellar population analysis of LAEs reported so far. In this subsection, we examine correlations among stellar population parameters, referring to the previous studies.

Table 9. Summary of Stellar Populations

Reference	z	M_{star} [$10^9 M_{\odot}$]	$E(B - V)_{\star}$ [mag]	Age [Myr]	Z [Z_{\odot}]	SFR [$M_{\odot} \text{ yr}^{-1}$]	τ [Myr]	Remarks
This Study	3.1	0.13	0.03	65	(0.2)	2.3	(∞)	(O09-1)
This Study	3.1	0.93 – 27	0.00 – 0.70	4.8 – 407	(0.2)	11 – 5.6×10^3	(∞)	(O09-2)
Gawiser et al. (2006)	3.1	0.5	0.0	90	(1)	6	(∞)	
Gawiser et al. (2007)	3.1	1.0	0.0	20	(1)	2	750	(G07)
Lai et al. (2008)	3.1	0.3	0.0	1.6×10^2	(1)	2	(∞)	(L08-1)
Lai et al. (2008)	3.1	9	0.0	1.6×10^3	(1)	6	(∞)	(L08-2)
Nilsson et al. (2007)	3.1	0.47	0.07	8.5×10^2	(0.005)	0.66	(∞)	
This Study	3.7	0.32	0.19	5.8	(0.2)	55	(∞)	(O09-1)
This Study	3.7	3.9 – 51	0.04 – 0.67	$1.4 - 9.1 \times 10^2$	(0.2)	21 – 3.5×10^4	(∞)	(O09-2)
Finkelstein et al. (2009)	4.5	0.084 – 6.1	0.02 – 0.41	2.5 – 500.0	0.005 – 1	1.30 – 5.78	$0.1 - 4 \times 10^3$	(F09)
Pirzkal et al. (2007)	4.00 – 5.76	0.007 – 1.8	0.0 – 0.16	1.0 – 20	0.005 – 2.5	—	1 – 12.5	(P07)
Lai et al. (2007)	5.7	17 – 39	0.150 – 0.225	720 – 900	(0.005)	—	(∞)	(L07)
Chary et al. (2005)	6.56	0.84	0.25	5	0.02	140	—	(C05)

NOTES: Values in parentheses are the assumed values in the literature.

REMARKS: (O09-1) K -undetected LAEs. (O09-2) K -detected LAEs. (G07) Their model has two stellar population components with different ages, and we adopt here the young component. The age of the old component is 2 Gyr. (L08-1) IRAC-undetected LAEs. (L08-2) IRAC-detected LAEs. (P07) The result with an exponentially decaying star formation history. In Figure 12, we show the results shown in Figure 4 of Castro Cerón et al. (2008). (F09) The result with an exponentially decaying star formation history. SFRs are calculated from model SEDs. (L07) In Figure 12, we show their results based on the assumption of constant star formation history and $0.005Z_{\odot}$. (C05) They calculate the SFR from the $H\alpha$ luminosity.

4.1.1 $M_{1500} - M_V$ versus M_{1500}

Figure 7 plots in large symbols rest-frame UV-to-optical colour ($M_{1500} - M_V$) against UV(= 1500Å) absolute magnitude (M_{1500}) for our LAEs. For conservative discussion, rest-frame 1500Å and V -band absolute magnitudes of our sample are derived from the best-fit SEDs, not from observed R - and K -band photometry (see details in Section 3.2).

For the 11 K -detected LAEs, nine are distributed in a similar region in the $M_{1500} - M_V$ versus M_{1500} plane to the LBGs. The remaining two are faint in M_{1500} and extremely red ($M_{1500} - M_V > 3$). Indeed, these are two of the four dusty LAEs, R1 and R2. On the contrary, the K -undetected LAEs, which occupy 96 % of our sample, have bluer $M_{1500} - M_V$ colours and much fainter M_{1500} magnitudes than the LBGs. The existence of K -bright LAEs suggests that not all LAEs at $z \sim 3$ are low-mass galaxies with blue colours and that LAEs are a heterogeneous population with wide ranges of stellar mass, age, and/or dust extinction (e.g., Lai et al. 2008; Finkelstein et al. 2008, 2009; Pentericci et al. 2009).

We also compare our LAEs with those in the literature at similar redshifts. The IRAC-detected LAEs by Lai et al. (2008) have similar $M_{1500} - M_V$ and M_{1500} to the LBGs. On the other hand, the NIR-undetected LAEs by Gawiser et al. (2007) and Lai et al. (2008) have as blue $M_{1500} - M_V$ colours and faint M_{1500} magnitudes as our K -undetected LAEs. The NIR-undetected LAE by Nilsson et al. (2007) has redder $M_{1500} - M_V$ than the other NIR-undetected LAEs, probably because their K -band image is relatively shallow (Table 1).

4.1.2 Stellar Mass versus M_V and M_{1500}

The left panel of Figure 8 shows stellar mass as a function of rest-frame V -band absolute magnitude for our LAEs calculated from best-fit SEDs. As expected, the K -detected LAEs have comparable stellar masses to the K -detected LBGs, spanning over $M_{\text{star}} \sim 10^9 - 10^{10.5} M_{\odot}$, while the K -undetected LAEs are much less massive, with $10^8 - 10^{8.5} M_{\odot}$.

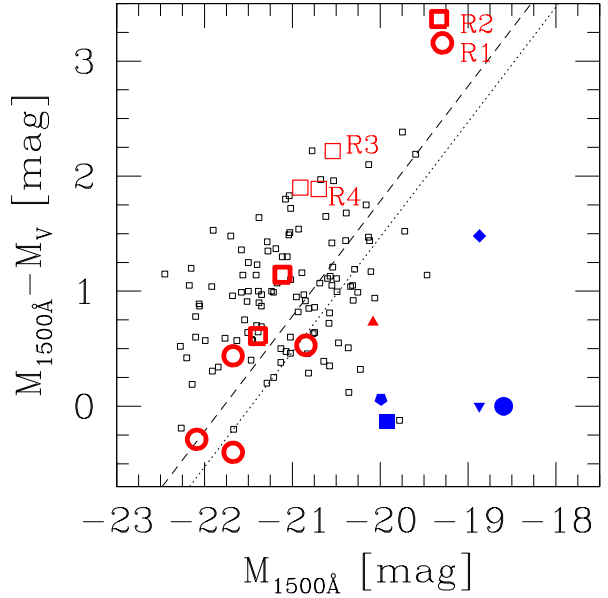


Figure 7. UV-to-optical colour ($M_{1500} - M_V$) versus rest-frame UV absolute magnitude (M_{1500}) for LAEs at $z = 3.1$ and 3.7 , and LBGs at $z \sim 3$. The red circles and squares indicate the K -detected LAEs at $z = 3.1$ and 3.7 , respectively, where those with spectroscopic confirmation are shown by bold symbols. Labels R1 – R4 indicate K -detected LAEs with extremely large dust extinction ($E(B - V)_{\star} \sim 0.65$). The blue filled circles and squares represent the K -undetected LAEs at $z = 3.1$ and 3.7 , respectively. The dotted and dashed lines correspond to the 3σ detection limit in the K band for LAEs at $z = 3.1$ and $z = 3.7$, respectively. The black squares are LBGs at $z \sim 3$ (Shapley et al. 2001; Papovich et al. 2001; Iwata et al. 2005), all of which are K -detected and spectroscopically confirmed. The blue upside-down pentagon and diamond represent composite LAEs at $z \sim 3.1$ (Gawiser et al. 2006) and $z \sim 3.15$ (Nilsson et al. 2007). The red and blue triangles indicate stacked IRAC-detected and undetected LAEs at $z = 3.1$ (Lai et al. 2008).

Our results broadly agree with previous studies. This figure shows that LAEs have a wide range of stellar mass.

The dashed lines indicate four mass-to-luminosity ratios. It is found that our K -undetected LAEs have slightly lower M_{star}/L_V ratios than the average K -detected LAEs and LBGs, suggestive of younger ages.

The right panel of Figure 8 plots stellar mass against rest-frame UV absolute magnitude. All but two of the K -detected LAEs are distributed in a region similar to the LBGs. The two exceptions are R1 and R2. The very faint M_{1500} magnitudes with respect to high M_{star} of R1 and R2 are mainly due to the extremely large dust extinction (see Table 7). The K -undetected LAEs are much fainter in UV wavelengths and much less massive than the LBGs.

4.1.3 Star Formation Rate versus M_{1500} and $L(\text{Ly}\alpha)$

The left panel of Figure 9 plots the star formation rate against the rest-frame UV absolute magnitude. For all objects SFRs are calculated from the best-fit SEDs. For the case of $E(B - V)_* = 0$, SFR approximately correlates with L_{1500} , and we plot this correlation with the dotted line using (Madau et al. 1998):

$$\text{SFR} [M_{\odot} \text{yr}^{-1}] = \frac{L_{1500} [\text{erg s}^{-1} \text{Hz}^{-1}]}{8 \times 10^{27}}. \quad (2)$$

Reflecting the wide range of $E(B - V)_*$, the K -detected objects are widely scattered above the dotted line. Some objects with very low extinction are located on the dotted line, while the four objects with extremely large extinction (R1 - R4) have SFRs more than two orders of magnitude higher than those expected from the observed M_{1500} . Except for R1 - R4, the K -detected LAEs have similar ranges of SFR and M_{1500} to the LBGs.

The K -undetected LAEs have SFRs of $1 - 100 M_{\odot} \text{yr}^{-1}$ and their offsets from the dotted line are within an order of magnitude because of the modest dust extinction. NB570- K -undetected is offset nearly an order of magnitude because of its relatively heavy dust extinction (Table 7).

The right panel of Figure 9 shows star formation rate versus observed Lyman α luminosity. Based on the relation between $\text{H}\alpha$ luminosity and star formation rate (Kennicutt 1998) under case B approximation (Brocklehurst 1971), star formation rate is related with Lyman α luminosity as:

$$\text{SFR} [M_{\odot} \text{yr}^{-1}] = 9.1 \times 10^{-43} L(\text{Ly}\alpha) [\text{erg s}^{-1}]. \quad (3)$$

The dotted line shows this relation. Star formation rates derived from SED fitting are found to be higher than those from equation (3). This can be explained by several reasons. $\text{Ly}\alpha$ photons can be attenuated by dust, and scattered in the interstellar and intergalactic medium. $\text{Ly}\alpha$ photons are resonantly scattered and heavily attenuated especially under a homogeneous ISM. Intrinsically, the $\text{Ly}\alpha$ emissivity is also affected by the age, metallicity, and IMF. In addition, the $L(\text{Ly}\alpha)$ of objects without spectroscopic redshifts tends to be underestimated due to the triangle shapes of the narrow-band filters. NB570- K -undetected lies well above equation (3), probably due to its relatively large $E(B - V)_*$.

4.1.4 Stellar Mass, Age, and $E(B - V)_*$ versus $\text{EW}(\text{Ly}\alpha)$

The top panel of Figure 10 shows stellar mass versus $\text{EW}(\text{Ly}\alpha)$. The K -detected objects are massive and have a wide range of $\text{EW}(\text{Ly}\alpha)$ over $20 - 220 \text{ \AA}$, but mostly in the range $\lesssim 100 \text{ \AA}$. On the other hand, the K -undetected objects are less massive and have consistently high values of $\sim 150 \text{ \AA}$. Considering that the K -undetected objects closely represent the whole LAE population, we can conclude from this figure that massive LAEs with high $\text{EW}(\text{Ly}\alpha)$ are rare.

There is a weak anti-correlation between stellar mass and $\text{EW}(\text{Ly}\alpha)$, if the four red objects (R1 - R4) are excluded. This anti-correlation is qualitatively consistent with the finding by Pentericci et al. (2009) in their LAE sample from $z \sim 3.5$ to 6 that more massive objects have in general smaller $\text{EW}(\text{Ly}\alpha)$.

This anti-correlation is not due to the Lyman α emission of more massive objects being more heavily absorbed by dust. For example, NB570-W-55371 has a small extinction ($E(B - V)_* = 0.04$) and a small $\text{EW}(\text{Ly}\alpha)$ (20 \AA), while NB503-S-94275 with a moderate extinction ($E(B - V)_* = 0.11$) has a large $\text{EW}(\text{Ly}\alpha)$ of 150 \AA and the $z = 3.7$ K -undetected objects with $E(B - V)_* = 0.19$ have a large $\text{EW}(\text{Ly}\alpha)$ of 130 \AA . Indeed, the bottom panel of Figure 10 shows no significant correlation between $E(B - V)_*$ and $\text{EW}(\text{Ly}\alpha)$. A cause of the anti-correlation may be that the geometry of dust in LAEs changes with stellar mass in the sense that more massive galaxies have a less clumpy distribution for some reason. As Neufeld (1991) points out, the fraction of $\text{Ly}\alpha$ photons escaping from a galaxy is higher for a clumpy cloud distribution than for a uniform distribution. This effect can explain the observed SEDs of LAEs at $z \sim 4.5$ (Finkelstein et al. 2009).

The middle panel of Figure 10 shows stellar age versus $\text{EW}(\text{Ly}\alpha)$. There seems to be a weak anti-correlation between stellar age versus $\text{EW}(\text{Ly}\alpha)$.

In the bottom panel of Figure 10, the small squares indicate the four averaged values of 38 LAEs at $z \sim 3.5 - 6$ by Pentericci et al. (2009). A probable reason for their very small $E(B - V)_*$ is that they have been selected using the LBG technique and thus have blue colours. The crosses represent the data for local star forming galaxies given in Giavalisco et al. (1996). In comparison to our LAEs, these local galaxies have on average smaller EWs. This might suggest a more uniform cloud distribution for local galaxies, if Neufeld (1991) picture is correct.

4.1.5 $\text{Ly}\alpha$ escape fraction versus $E(B - V)_{\text{gas}}$

We define the $\text{Ly}\alpha$ escape fraction $f_{\text{esc}}(\text{Ly}\alpha)$ by:

$$f_{\text{esc}}(\text{Ly}\alpha) = \frac{L_{\text{obs}}(\text{Ly}\alpha) [\text{erg s}^{-1}]}{L_{\text{int}}(\text{Ly}\alpha) [\text{erg s}^{-1}]}, \quad (4)$$

where $L_{\text{int}}(\text{Ly}\alpha) [\text{erg s}^{-1}] = 1.1 \times 10^{42} \text{ SFR} [M_{\odot} \text{yr}^{-1}]$, equivalent to equation (3), is the intrinsic $\text{Ly}\alpha$ luminosity computed from the SFR on the assumption of case B. Since the SFR is derived from our SED fitting, it has been corrected for dust extinction. Then $f_{\text{esc}}(\text{Ly}\alpha)$ is plotted against $E(B - V)_{\text{gas}}$ in Figure 11. As for our results, $E(B - V)_{\text{gas}} = E(B - V)_*/0.44$ (Calzetti et al. 2000). A strong negative correlation is seen between the two quantities for our objects. The K -undetected LAEs, whose dust extinction is modest,

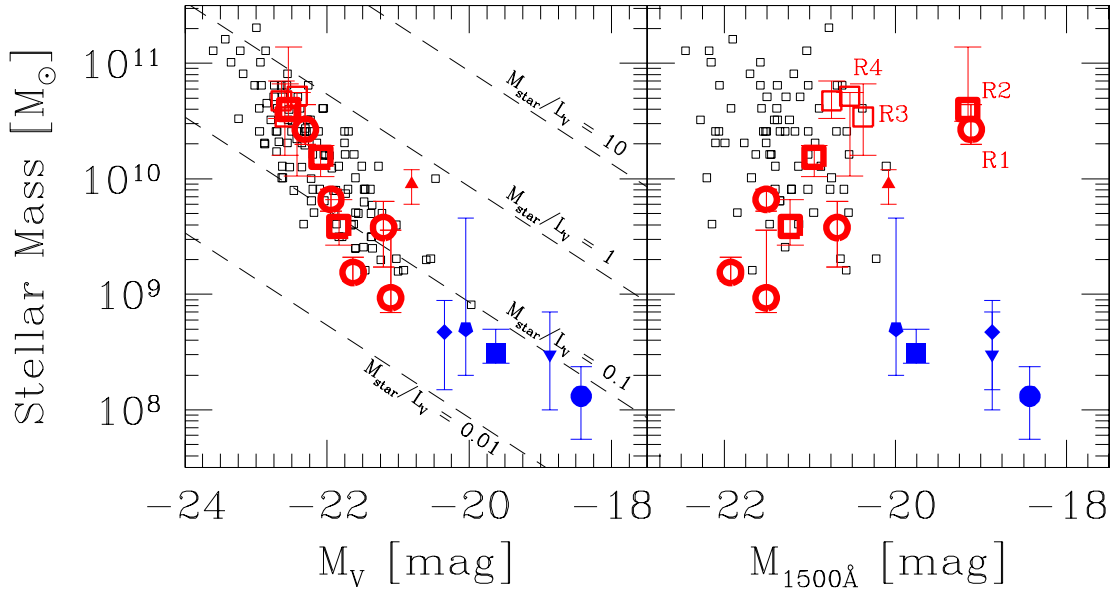


Figure 8. **Left:** Stellar mass versus rest-frame V -band absolute magnitude. All symbols are the same as in Figure 7. Black dashed lines correspond to four mass-to-luminosity ratios normalised by the solar value. **Right:** Stellar mass versus rest-frame UV absolute magnitude. All symbols are the same as in Figure 7.

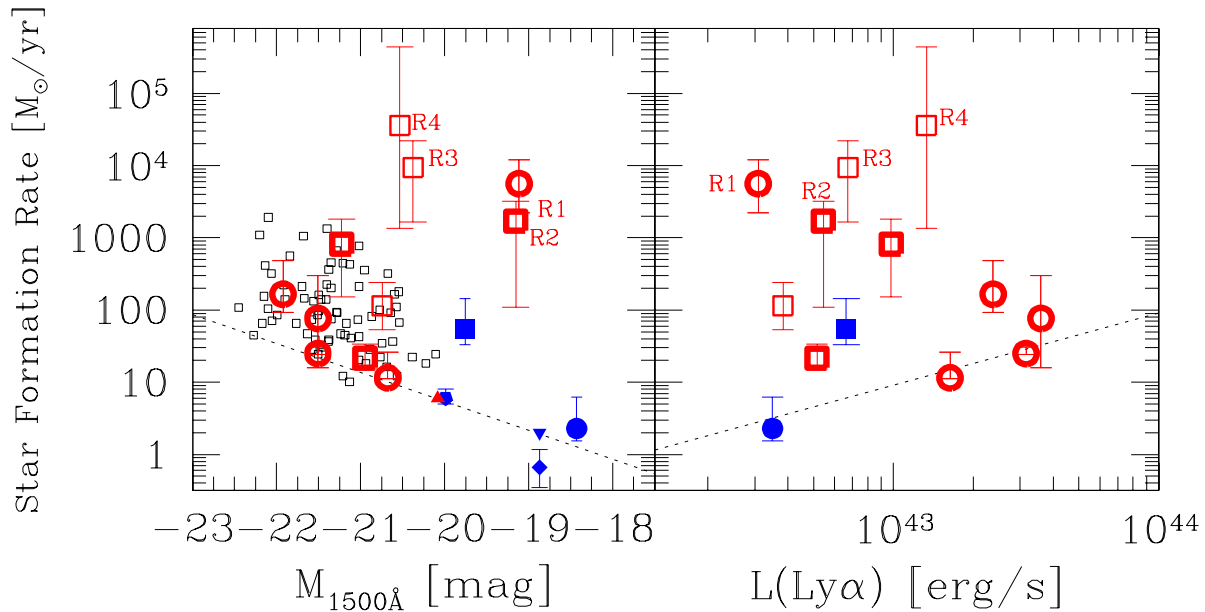


Figure 9. **Left:** Star formation rate derived from SED fitting, plotted against the UV absolute magnitude. All symbols are the same as in Figure 7. The dotted line shows the relation between the UV luminosity and the star formation rate (Madau et al. 1998). **Right:** Star formation rate derived from SED fitting, plotted against the Ly α luminosity. All symbols are the same as in Figure 7. The dotted line shows the relation between the Ly α luminosity and the star formation rate.

have relatively large $f_{\text{esc}}(\text{Ly}\alpha)$ of $\simeq 0.1 - 1$, while the K -detected LAEs, whose $E(B - V)_{\text{gas}}$ can be as large as 1.5, have $f_{\text{esc}}(\text{Ly}\alpha) \sim 3 \times 10^{-4} - 1$. R1 – R4 have the smallest escape fractions.

We discuss implications of this negative correlation. Assuming f_{ν} = constant over 1200 – 1500 Å, we obtain $L_{\text{obs}}(\text{Ly}\alpha) \equiv \text{EW}(\text{Ly}\alpha)(c/\lambda_0^2)L_{1500,\text{obs}}$ as:

$$L_{\text{obs}}(\text{Ly}\alpha) = \text{EW}(\text{Ly}\alpha) \frac{c}{\lambda_0^2} L_{1500} 10^{-0.4R(\lambda_0)E(B-V)_{\text{gas}}}, \quad (5)$$

where $\lambda_0 = 1216 \text{ \AA}$, and $R(\lambda_0) = 0.44k'(\lambda_0) \simeq 5.27$ is the selective extinction at 1216 Å for Calzetti extinction law. Combining this equation with equations (2) and (3), we rewrite equation (4) as:

$$f_{\text{esc}}(\text{Ly}\alpha) = \frac{8 \times 10^{27}}{1.1 \times 10^{42}} \frac{c}{\lambda_0^2} \cdot \text{EW}(\text{Ly}\alpha) \cdot 10^{-0.4R(\lambda_0)E(B-V)_{\text{gas}}} \quad (6)$$

The dashed line in Figure 11 corresponds to this equation for $\text{EW}(\text{Ly}\alpha) = 68 \text{ \AA}$, the value of $\text{EW}(\text{Ly}\alpha)$ expected for

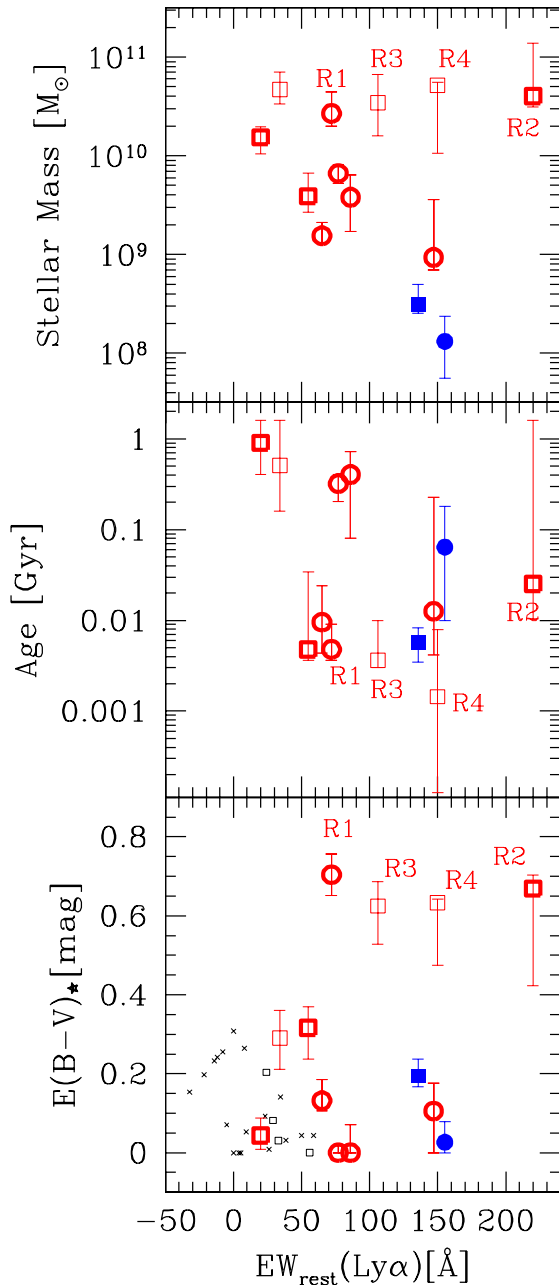


Figure 10. **Top:** Stellar mass derived from SED fitting versus rest-frame Ly α equivalent width. All symbols are the same as in Figure 7. **Middle:** Stellar age derived from SED fitting versus rest-frame Ly α equivalent width. All symbols are the same as in Figure 7. **Bottom:** Dust reddening $E(B - V)_*$ derived from SED fitting versus rest-frame Ly α equivalent width. The black small squares are taken from Pentericci et al. (2009). The crosses are star-forming galaxies in the local universe taken from Giavalisco et al. (1996). The remaining symbols are the same as in Figure 7.

$f_{\text{esc}}(\text{Ly}\alpha) = 1$ when $E(B - V)_{\text{gas}} = 0$. In other words, we assume here that the absorption fractions of Ly α photons and continuum photons near Ly α wavelength are identical irrespective of $E(B - V)_{\text{gas}}$. Clearly, this assumption is not valid for uniform ISM, since Ly α photons are more heavily absorbed before escaping from the galaxy. In this sense, it

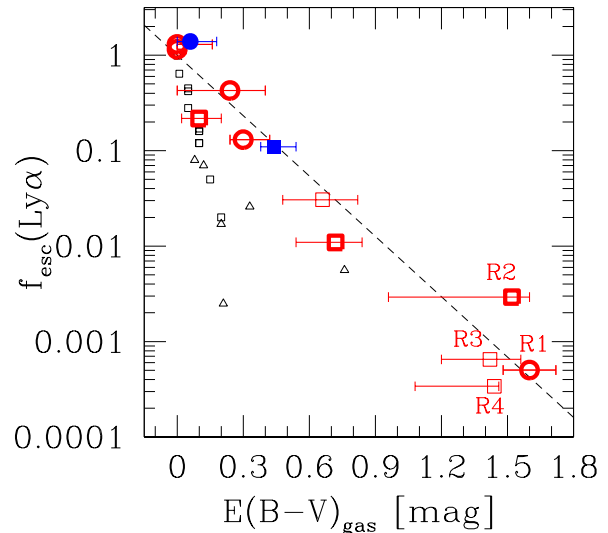


Figure 11. Ly α escape fraction versus $E(B - V)_{\text{gas}}$. As for our results, $E(B - V)_{\text{gas}} = E(B - V)_*/0.44$ (Calzetti et al. 2000). The triangles are star-forming galaxies in the local universe (Atek et al. 2008), and the black small squares are $z \sim 3$ LBGs (Verhamme et al. 2008). The remaining symbols are the same as in Figure 7. The dashed line corresponds to equation (6).

is interesting that almost all of our LAEs are on the dashed line. Similar to the bottom panel of Figure 10, which shows no significant correlation between $E(B - V)_*$ and $\text{EW}(\text{Ly}\alpha)$, this result also suggests that in heavily obscured LAEs the absorption of Ly α photons is not as strong as expected for uniform ISM.

Our result is consistent with the result of Valls-Gabaud (1993), who has studied nearby starburst galaxies and showed that most of them present normal Ly α emission consistent with case B recombination. This implies that the effect of resonant scattering is not so strong.

Finkelstein et al. (2009) have studied $z \sim 4.5$ LAEs considering their dust geometries by introducing the q parameter as the ratio of the optical depth for Ly α to that for UV continuum. Our results suggest that Ly α photons and UV continuum photons near Ly α wavelength are equally attenuated by dust. This corresponds to $q = 1$. Interestingly, Finkelstein et al. (2009) have found that, although three objects have $q > 1$ and two have $q = 1$, the remaining nine have $q < 1$. This might mean that the dust effect on Ly α photons is more important at higher redshift.

The black small squares represent the results for 11 LBGs at $z \sim 3$ by Verhamme et al. (2008). Although they also show a negative correlation, its slope is steeper than the dashed line. This means that for a given $E(B - V)_{\text{gas}}$, Ly α photons are more strongly absorbed in comparison with LAEs. Similarly, local star-forming galaxies (open triangles, Atek et al. 2008) also tend to have lower $f_{\text{esc}}(\text{Ly}\alpha)$.

4.1.6 Specific Star Formation Rate versus Stellar Mass: Comparison with other high- z galaxy populations

We plot in Figure 12 the specific star formation rate (sSFR $\equiv \text{SFR}/M_{\text{star}}$) against the stellar mass for our LAEs and other high-redshift galaxies selected by various photometric

selection methods, in order to compare the mass scale and star-formation activity between the high- z galaxy populations. Also plotted are LAEs over a wide range of redshift taken from the literature. The data plotted are summarised below:

LAEs

Large blue filled circle and large blue filled square: K -undetected (stacked) LAEs in our sample at $z = 3.1$ and 3.7 , respectively. Large red open circles and large red open squares: K -detected LAEs in our sample at $z = 3.1$ and 3.7 , respectively, where those with a spectroscopic redshift are shown by bold symbols. Blue filled inverse pentagon: 18 stacked LAEs at $z = 3.1$ (Gawiser et al. 2006). Blue filled diamond: 23 stacked LAEs at $z = 3.15$ (Nilsson et al. 2007). Blue filled pentagon: 52 stacked LAEs at $z = 3.1$ (Gawiser et al. 2007). Blue filled triangle and red filled triangle: 76 IRAC-undetected and 18 IRAC-detected LAEs at $z = 3.1$, respectively (Lai et al. 2008). Red open triangles: three IRAC-detected LAEs at $z = 5.7$ (Lai et al. 2007). Blue open diamonds and red open diamonds: IRAC-undetected and IRAC-detected LAEs at $z = 4.5$, respectively (Finkelstein et al. 2009). Blue open pentagons: nine LAEs at $z \sim 5$ (Pirzkal et al. 2007). Red open hexagon: a LAE at $z = 6.56$ (Chary et al. 2005).

LBGs

Small open squares: K -detected LBGs with spectroscopic redshifts at $z \sim 3$ (Shapley et al. 2001: $K_s < 24.3$, Papovich et al. 2001: $K_s < 23.8$, Iwata et al. 2005: $K < 25.4$). The distribution of their stellar masses has a lower cutoff at $\sim 10^9 M_\odot$, which roughly corresponds to the limiting K magnitudes.

DRGs

Small open circles: DRGs at $z \sim 2 - 3$ selected by $J - K > 1.3$ (van Dokkum et al. 2004), which are thought to be either passively evolving massive galaxies or dusty starburst galaxies. Since they are all K -bright, their stellar masses are higher than $\sim 10^{11} M_\odot$.

SMGs

Asterisks: submillimetre galaxies (SMGs) at $z \sim 2$ (Borys et al. 2005; Chapman et al. 2005), which are thought to be massive, dusty starburst galaxies.

Galaxies with Photometric Redshifts

Black and magenta dots: I -band and K -band selected galaxies at $2.5 < z < 3.5$, respectively, whose redshifts are estimated from the photometric redshift technique (Feulner et al. 2005)⁶.

We first focus on the stacked LAEs (blue filled symbols), which should closely represent the whole LAE population. The stellar masses of the stacked LAEs span over $10^8 - 10^9 M_\odot$ (the individually measured LAEs in Pirzkal et al. (2007) have slightly lower masses), while those of the LBGs, DRGs, SMGs, and photo- z galaxies are $10^9 - 10^{11} M_\odot$, $10^{11} - 10^{12} M_\odot$, $10^{11} - 10^{12} M_\odot$, and $10^{8.5} - 10^{11} M_\odot$, respectively. Thus, LAEs are the least massive galaxy population among those discussed here. This implies that a significant fraction

of low-mass galaxies beyond the limits of broad-band surveys have Lyman α emission strong enough to be detected in narrow-band surveys. Note, however, that this does not rule out the existence of low-mass galaxies with weak or without Lyman α emission.

The sSFRs of the stacked LAEs span over two orders of magnitude, from 10^{-9} to 10^{-7} yr^{-1} , although each measurement has large uncertainties. This range of sSFR is similar to that of the LBGs, implying that these two galaxy populations have similar growth rates of stellar mass in spite of the large difference in M_{star} . In contrast, the stacked LAEs appear to have higher sSFRs than the DRGs, SMGs, and photo- z selected galaxies. Since the shaded region has not been explored, the existence of low-mass galaxies with very low sSFRs is not ruled out.

We then discuss the K - and IRAC-detected LAEs. Our K -detected LAEs are distributed in a similar region to the LBGs (all are K -detected), except for the four massive LAEs with very high sSFRs labelled as R1 – R4. Finkelstein et al. (2009)'s IRAC-detected LAEs are distributed in a similar region to the photo- z galaxies, with relatively low stellar masses, which reflects the deep IRAC Ch1 limit. On the other hand, Lai et al. (2007) IRAC-detected LAEs at $z = 5.7$ are as massive as the LBGs due to the relatively shallow limiting magnitude. Overall, the K - and IRAC-detected LAEs are not discriminated from the LBGs and photo- z galaxies in the sSFR versus M_{star} plane.

4.2 Properties of Red LAEs

As seen in the previous subsection, the four red LAEs (R1 – R4) behave quite differently from the other LAEs in most of the two-parameter spaces. They have large stellar masses and high SFRs for relatively faint UV absolute magnitudes (Figure 9). They deviate from a negative correlation between M_{star} and EW(Ly α) seen in the majority of LAEs (top panel of Figure 10). They have large EWs in spite of extremely large $E(B - V)_*$ (bottom panel of Figure 10). Finally, they have much higher sSFRs than other galaxies with similar stellar masses (Figure 12). These results collectively suggest that they are not just massive LAEs, but may belong to a special class of galaxies involving obscured starburst. In this subsection, we further investigate their properties in conjunction with MIPS $24\mu\text{m}$ data and the IMACS spectra.

4.2.1 Star Formation Rates based on MIPS Photometry

All four objects have been imaged with MIPS at $24\mu\text{m}$ in the SpUDS. We find that R4 (NB570-W-59558) is detected at $\simeq 5\sigma$ level ($m_{24\mu\text{m}} = 19.3$) while the remaining three are fainter than the 3σ limit ($m_{24\mu\text{m}} = 19.8$). Note that none of the four has a counterpart either in the XMM-Newton X-ray catalogue (Ueda et al. 2008) with a detection limit of $f(0.5 - 2 \text{ keV}) = 6 \times 10^{-16} \text{ erg cm}^{-2} \text{ s}^{-1}$, or in the VLA radio catalogue (Simpson et al. 2006) with a detection limit of $f(1.4 \text{ GHz}) = 100\mu\text{Jy}$. All four are out of the SCUBA Half-Degree Extragalactic Survey (SHADES; Coppin et al. 2006).

We cannot completely exclude the possibility that the MIPS photometry of R4 suffers from confusion, because there are two objects near R4 in the optical wavebands with

⁶ <http://www.pik-potsdam.de/members/feulner/research/cosmology/electronic-data>

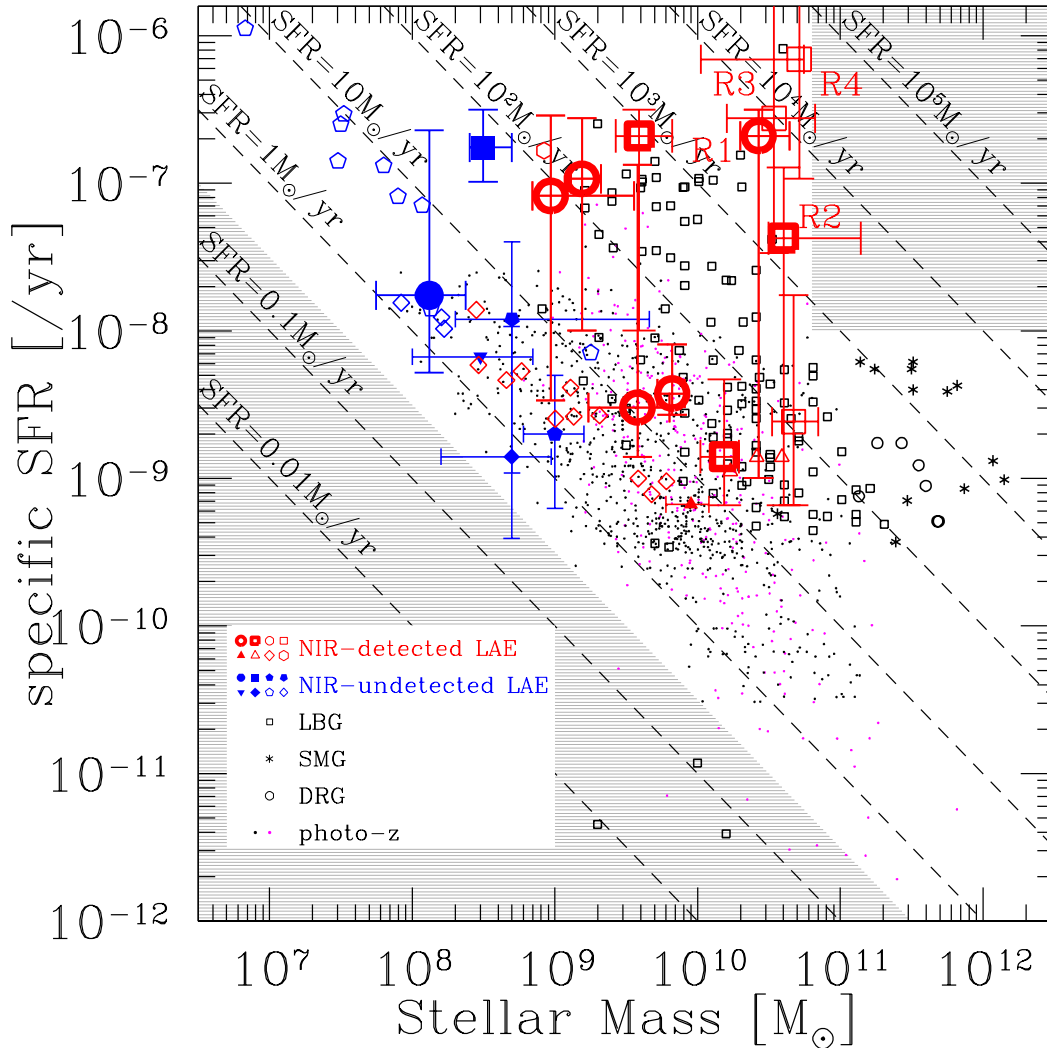


Figure 12. Stellar mass versus specific star formation rate ($=\text{SFR}/\text{stellar mass}$). The dashed lines represent $\text{SFR} = 0.01 - 10^5 M_{\odot} \text{yr}^{-1}$ from left to right. The blue filled pentagon represents a stacked LAE of 52 objects at $z = 3.1$ (Gawiser et al. 2007). The red and blue open diamonds are 14 LAEs $z \sim 4.5$ with and without IRAC-detection (Finkelstein et al. 2009, private communication). The blue open pentagons are LAEs at $z \sim 5$ (Pirzkal et al. 2007; Castro Cerón et al. 2008). The red open triangles are three IRAC-detected LAEs at $z = 5.7$ (Lai et al. 2007). The red open hexagon is a lensed LAE at $z = 6.56$ (Chary et al. 2005). The star marks are SMGs from Borys et al. (2005) and Chapman et al. (2005). The small circles are DRGs from van Dokkum et al. (2004). The black and magenta dots are I -band and K -band detected photo- z samples respectively (Feulner et al. 2005). The remaining symbols are the same as in Figure 7. There is no object in the region of the high stellar mass and sSFR (shaded region in the top-right corner). The lower-left shaded region corresponds to quiescent low-mass objects, almost all of which are missed so far.

a separation of about 1.8 and 3.8 arcsec, respectively. In the following, we assume that possible source confusion does not significantly affect the MIPS photometry.

We use the template SEDs of starburst galaxies given in Lagache et al. (2003)⁷ and Vega et al. (2008)⁸ to estimate SFRs from the observed $24\mu\text{m}$ flux density. As will be shown below, the SFRs thus estimated have considerably large uncertainties because $24\mu\text{m}$ corresponds to near the blue end of dust emission for our objects. We use one template ($L_{\text{IR}}[L_{\odot}] = 10^{12}$) from Lagache et al. (2003), and templates

of 14 starburst-dominated ULIRGs⁹ from Vega et al. (2008). The range of their $\log(L_{\text{IR}}[L_{\odot}])$ is from 11.39 – 12.24. We redshift them at $z = 3.1$ and 3.7 and find scaling relations between $m_{24\mu\text{m}}$ and L_{IR} for individual templates. We then derive SFRs from individual L_{IR} using the relation between SFR_{IR} and L_{IR} given in Kennicutt (1998):

$$\text{SFR}_{\text{IR}} [M_{\odot}\text{yr}^{-1}] = 1.7 \times 10^{-10} L_{\text{IR}}[L_{\odot}]. \quad (7)$$

We obtain $\text{SFR}_{\text{IR}} \simeq 4.2 \times 10^3 - 2.0 \times 10^4 [M_{\odot}\text{yr}^{-1}]$ (median $\text{SFR}_{\text{IR}} \simeq 7.4 \times 10^3 [M_{\odot}\text{yr}^{-1}]$) for R4 and upper limits for

⁷ <http://www.ias.u-psud.fr/irgalaxies/model.php#SED>

⁸ <http://adlibitum.oat.ts.astro.it/silva/grasil/modlib/modlib.html>

⁹ IR 12112+0305, UGC 9913, IR 10565+2448, IZW 107, IR 10173+0828, Arp 299, UGC 4881, IC 1623, UGC 8387, UGC 2369, IIZW 35, IC 5298, Arp 148, UGC 6436.

the remaining three of $1.1 \times 10^3 - 4.3 \times 10^3 [M_{\odot} \text{yr}^{-1}]$ (median $\simeq 1.5 \times 10^3 [M_{\odot} \text{yr}^{-1}]$) for $z = 3.1$, and $2.8 \times 10^3 - 1.3 \times 10^4 [M_{\odot} \text{yr}^{-1}]$ (median $\simeq 4.9 \times 10^3 [M_{\odot} \text{yr}^{-1}]$) for $z = 3.7$. The variation of SFR_{IR} among the 15 templates is thus a factor $\simeq 4$.

In the left panel of Figure 13, we compare the SFR derived from the SED fitting ($\text{SFR}_{\text{SEDfit}}$) with the sum of the SFRs derived from the observed UV and IR luminosities ($\text{SFR}_{\text{UV+IR}}$). We do not find inconsistency between $\text{SFR}_{\text{SEDfit}}$ and $\text{SFR}_{\text{UV+IR}}$, although the $\text{SFR}_{\text{UV+IR}}$ of three objects is an upper limit and thus the constraint on the consistency is not so strong. R4 is detected at $24\mu\text{m}$ and its $\text{SFR}_{\text{UV+IR}}$ is comparable to those of SMGs and DRGs. These results support our inference that the four red LAEs are massive, dusty starburst galaxies. They can be detected with SCUBA2/JCMT and Herschel.

In the right panel of Figure 13, the ratio of SFR_{IR} to $\text{SFR}_{\text{SEDfit}}$ is shown. The dotted line corresponds to $\text{SFR}_{\text{total}} = \text{SFR}_{\text{IR}}$, i.e., all of the intrinsic UV emission is re-emitted from dust. Only R4 is detected at $24\mu\text{m}$ and has $\text{SFR}_{\text{IR}}/\text{SFR}_{\text{total}} \simeq 0.2$, while the other three have upper limits of $0.5 - 3$. This result may suggest that the contribution of the obscured star formation to the total star formation is not necessarily very large.

We make median-stacked MIPS $24\mu\text{m}$ images of the LAEs fainter than $K(3\sigma)$ at each redshift (211 for $z = 3.1$ and 70 for $z = 3.7$). We find that both are fainter than $m_{24\mu\text{m}}(3\sigma)$, obtaining upper limits of $\text{SFR}_{\text{IR}} = 1.0 \times 10^2$ (5.8×10^2) $[M_{\odot} \text{yr}^{-1}]$ ¹⁰ for the $z = 3.1$ (3.7) LAEs. The results are plotted in blue symbols in Figure 13. We cannot place strong constraints either on the consistency between $\text{SFR}_{\text{SEDfit}}$ and $\text{SFR}_{\text{UV+IR}}$ (left panel) or on the fraction of obscured star formation (right panel).

Note that we cannot completely exclude AGN-contaminated objects from our sample. In particular, the MIPS detection for R4 may imply that it has a significant amount of AGN contribution. In this case, the SFRs calculated above are overestimated.

4.2.2 Velocity Widths of Lyman α Emission

As described in Section 2.5, we performed spectroscopy of two red LAEs (R1 and R2) with IMACS on Magellan, and confirmed them to be real LAEs. We obtain a Ly α line width of $v_{\text{FWHM}} = 205 \pm 129 \text{ km s}^{-1}$ for R1, and $v_{\text{FWHM}} = 629 \pm 201 \text{ km s}^{-1}$ for R2, after correction for instrumental broadening on the assumption that their intrinsic profiles are Gaussian. Venemans et al. (2005) have reported that the typical FWHM of the Ly α line of LAEs is 340 km s^{-1} (see also Taniguchi et al. 2005; Kashikawa et al. 2006; Tapken et al. 2007). The velocity width of R1 is similar to this value. On the other hand, R2 has twice as large a value, and it might suggest that this object involves gas outflows (e.g., Taniguchi & Shioya 2000), that it is a merger of two objects with a large relative velocity, or that it has a heavily obscured AGN.

¹⁰ These are median values of the cases with the 15 SB-dominated ULIRGs. The range of the upper limits of SFR_{IR} are $73 - 2.9 \times 10^2 [M_{\odot} \text{yr}^{-1}]$ for $z = 3.1$, and $3.3 \times 10^2 - 1.6 \times 10^3 [M_{\odot} \text{yr}^{-1}]$ for $z = 3.7$.

4.2.3 Comparison with Other Red LAEs and Local Starburst Galaxies

We compare in Figure 14 the SEDs of R1 and R2 (both have a spectroscopic redshift) with those of the three local starburst galaxies Arp 220, M82 (Silva et al. 1998), and IR10565+2448, which has no AGN contribution to its IR luminosity (Vega et al. 2008), and Mrk 231 (Polletta et al. 2007), which is considered to be a local starburst galaxy with a heavily obscured AGN. Also plotted are two SMGs with strong Ly α emission recently discovered by Capak et al. (2008) and Coppin et al. (2009).

Over the rest-frame UV to NIR wavelengths, R1 resembles Arp 220 and IR10565+2448 more closely while R2 resembles Mrk 231, and both are almost one order of magnitude brighter than M82. This might indicate that R1 is a pure star-forming system, while R2 is a star-forming galaxy with an obscured AGN. The SEDs of R1 and R2 including upper limits at the MIPS and VLA wavelengths are consistent with them being dusty starburst galaxies. The two SMGs are even brighter than our objects, Arp 220, Mrk 231, and IR10565+2448, and have significantly bluer SEDs.

Table 10 summarises their stellar populations. R1 and R2 are found to have similar stellar masses to Arp 220, IR10565+2448, and the two SMGs (For the $z = 4.55$ object we adopt the values for the diffuse component); M82 is ~ 100 times less massive. The $E(B - V)_{\star}$ values of R1 and R2 are close to that of Arp 220, and the other objects are less obscured. Ages are not strongly constrained, but all objects appear to be young. The SFRs of R1 and R2 are several times higher than that of Arp 220 and are comparable to that of the $z = 4.55$ SMG. Thus Table 10 leads us to concluding that R1 and possibly R2 are high- z counterparts of present-day ULIRGs.

The number density of the red LAEs (R1 – R4) in our sample is $\sim 2 \times 10^{-6} \text{ Mpc}^{-3}$ at $z = 3.1$, and $\sim 7 \times 10^{-6} \text{ Mpc}^{-3}$ at $z = 3.7$, respectively. These values are about one order of magnitude lower than that of SMGs at $z \sim 2 - 3$ (Chapman et al. 2005). If red LAEs and SMGs are both massive dusty starburst galaxies, then the difference in the number density would imply that dusty starburst galaxies emit Ly α photons in only a short time in their starburst phase. In that time the distribution of dust in the galaxy might be clumpy so that Ly α photons can escape relatively easily.

Note that we cannot rule out the existence of obscured AGNs in our red LAEs. Actually, Geach et al. (2009) have reported that all AGN in the Ly α blobs in the $z = 3.09$ proto-cluster in the SSA22 field appear to be heavily obscured. If the contribution from AGNs to the SEDs is significant, our discussion about their stellar populations will have to be modified. Even in such cases, however, our finding of R1 – R4 demonstrates that Ly α surveys can detect galaxies with very red UV-to-optical SEDs, which are difficult to be identified by other photometric selection methods.

4.3 Contribution of LAEs to the Stellar Mass Density and the Cosmic Star Formation Rate Density

We estimate the contribution from LAEs (both K -detected and K -undetected) to the cosmic stellar mass density at

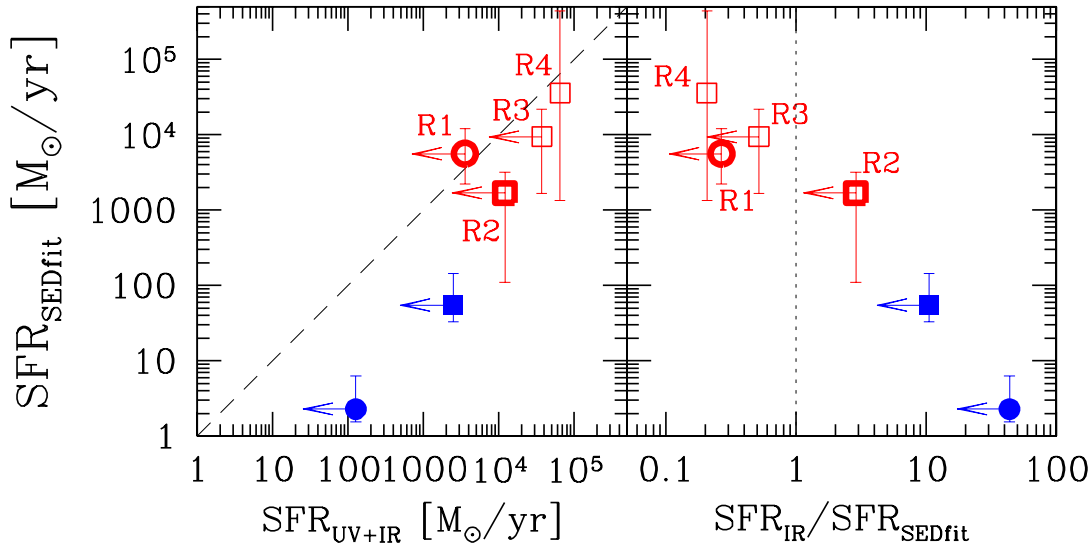


Figure 13. *Left:* Comparison of the SFR derived from the SED fitting with the SFR derived from the observed UV+IR luminosities. The dashed line corresponds to $\text{SFR}_{\text{SEDFit}} = \text{SFR}_{\text{UV+IR}}$. The red symbols are the four red LAEs. The blue filled circle and square are the K -undetected LAEs at $z = 3.1$ and $z = 3.7$, respectively. *Right:* Fraction of obscured SFR ($\text{SFR}_{\text{IR}}/\text{SFR}_{\text{SEDFit}}$), plotted against $\text{SFR}_{\text{SEDFit}}$. The dotted line is the equality line. All symbols are the same as in the left panel.

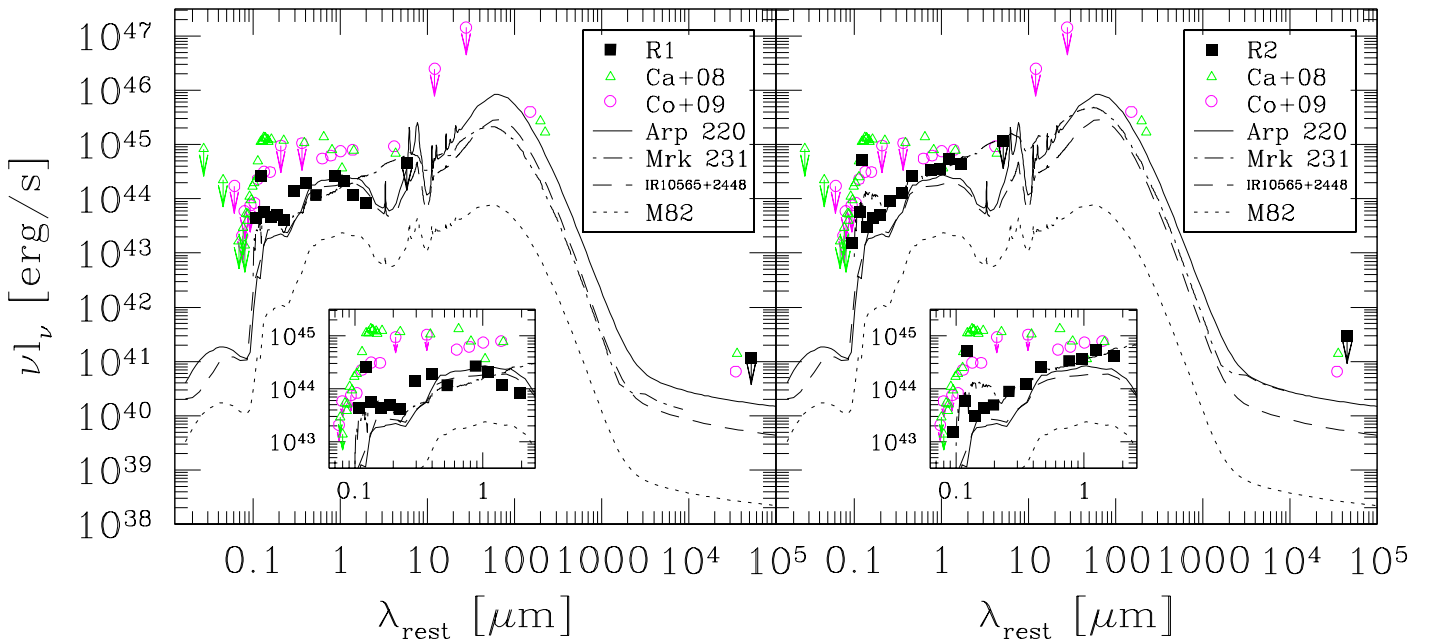


Figure 14. Multiwavelength SEDs of two spectroscopically confirmed red LAEs (black squares): NB503-N-21105 (R1; left) and NB570-N-32295 (R2; right). Also plotted are the SEDs of Arp 220 (solid line), M82 (dotted line), both from Silva et al. (1998), IR10565+2448 (dashed line) from Vega et al. (2008), Mrk 231 (chain line) from Polletta et al. (2007), Ly α -emitting SMGs at $z = 4.87$ (Coppin et al. 2009, magenta circles) and at $z = 4.547$ (Capak et al. 2008, green triangles). The inner panels are a zoom up over the wavelength range from UV to near-infrared.

$z = 3.1$ and 3.7 , by dividing the total stellar mass of LAEs by the comoving volume searched by each narrow band. The total stellar mass at each redshift is defined as the stellar mass of the stacked LAEs multiplied by their number, plus the sum of the K -detected LAEs' masses. We obtain $1.4 \times 10^5 [M_{\odot} \text{Mpc}^{-3}]$ for $z = 3.1$ LAEs, and $5.2 \times 10^5 [M_{\odot} \text{Mpc}^{-3}]$

for $z = 3.7$ LAEs. These values can be regarded as lower limits of the contribution to the cosmic stellar mass density.

Grazian et al. (2007) have obtained the stellar mass densities of LBGs and DRGs at $z \sim 3$ by integrating their stellar mass functions, to be $\sim 1 \times 10^7 [M_{\odot} \text{Mpc}^{-3}]$ for LBGs, and $\sim 7 \times 10^6 [M_{\odot} \text{Mpc}^{-3}]$ for DRGs. The stellar mass densities of our LAEs are 1 – 3 % of that of LBGs+DRGs.

Table 10. Comparison of stellar populations of dusty starburst galaxies

Object	M_{star} [M_{\odot}]	$E(B - V)_{\star}$ [mag]	Age [Myr]	SFR [$M_{\odot} \text{ yr}^{-1}$]	Reference	Remark
NB503-N-21105 (R1)	2.7×10^{10}	0.70	4.8	5.6×10^3	This Study	
NB570-N-32295 (R2)	4.0×10^{10}	0.67	25	1.7×10^3	This Study	
Arp 220	2.5×10^{10}	0.6	(50)	5.8×10^2	Silva et al. (1998)	1
M 82	2×10^8	0.28	(50)	5.5	Silva et al. (1998)	1
IR10565+2448	2.3×10^{10}	—	81	281.5	Vega et al. (2008)	2
$z = 4.87$ SMG	$\lesssim 5 \times 10^{10}$	0.37	40	5×10^2	Coppin et al. (2009)	3
$z = 4.55$ SMG diffuse	2×10^{10}	0.37	7.6	4.2×10^3	Capak et al. (2008)	4

¹ They have used a library generated with GRASIL (Silva et al. 1998) to make model SEDs. The stellar mass shown here is the gas mass which was converted into stars during the most recent burst (see below). We calculate the colour excess $E(B - V)_{\star}$ from the optical depth in the B band they have reported ($\tau_B \sim 2.8$ for Arp 220, and $\tau_B \sim 1.3$ for M82), using Calzetti et al. (2000) extinction curve. For both objects, they assumed that the SFR increased in the first 3 Gyr and then smoothly decreased until an age of 13 Gyr, followed by a starburst which occurred at 5×10^7 years ago. The SFRs shown here are the ones averaged over the last 5×10^7 years.

² They have used a library generated with GRASIL (Silva et al. 1998) to make model SEDs. The assumed an exponentially decaying starburst. For age and stellar mass, we adopt the age of the burst (age_b) and the mass of stars created during the burst (M_{\star}^b). The SFR we adopt is the one averaged over the period of the burst.

³ They have used the stellar population model of Bruzual & Charlot (1993), the Calzetti et al. (2000) extinction law, and either a constant or single-burst star formation history, assuming $Z = Z_{\odot}$. They have derived its stellar mass from an upper limit of the rest-frame K -band luminosity and the mass-to-luminosity ratio obtained by Borys et al. (2005). They have reported the dust extinction amount in the V band to be $A_V \sim 1.5$. We calculate its colour excess $E(B - V)_{\star}$ using Calzetti et al. (2000) law. They have estimated the SFR by dividing the stellar mass by an age of ~ 100 Myr.

⁴ Since this object has a UV bright knot and a diffuse component, they have analysed separately the knot and the diffuse component. We adopt here the values for the diffuse component. They have used the stellar population model of Bruzual & Charlot (2003), Salpeter (1955) IMF, Calzetti et al. (2000) extinction law, and a single-burst star formation history, assuming $Z = Z_{\odot}$. They have reported the dust extinction in the V band, and we calculate the colour excess $E(B - V)_{\star}$ using Calzetti et al. (2000) law.

Similarly, we estimate the contribution from LAEs (both K -detected and K -undetected) to the cosmic star formation rate density, where the total star formation rate is computed as the star formation rate of the stacked objects multiplied by their number, plus the sum of the K -detected LAEs' star formation rates. We obtain $8.2 \times 10^{-3} [M_{\odot} \text{ yr}^{-1} \text{ Mpc}^{-3}]$ for $z = 3.1$ LAEs, and $1.3 \times 10^{-1} [M_{\odot} \text{ yr}^{-1} \text{ Mpc}^{-3}]$ for $z = 3.7$ LAEs. The cosmic star formation density due to all galaxies is estimated to be $\log \dot{\rho}_{\star} \sim 0.18 [M_{\odot} \text{ yr}^{-1} \text{ Mpc}^{-3}]$ at $z = 3.1$, and $\log \dot{\rho}_{\star} \sim 0.14 [M_{\odot} \text{ yr}^{-1} \text{ Mpc}^{-3}]$ at $z = 3.7$ (Hopkins et al. 2006). Thus the lower limit to the contribution from LAEs is about 0.04 – 1 %.

It is interesting to note that for our LAEs both the cosmic star formation rate and the stellar mass density are higher at $z = 3.7$. This may mean that at higher redshift a higher fraction of galaxies are actively forming stars, or that the fraction of galaxies with Lyman α EWs large enough to be selected as LAEs increases with redshift.

5 SUMMARY AND CONCLUSIONS

In this paper, we have investigated the stellar populations of LAEs at $z = 3.1$ and 3.7 found in 0.65 deg^2 of the SXDF, based on deep, rest-frame UV-to-optical photometry from three surveys made with Suprime-Cam/Subaru, WFCAM/UKIRT, and IRAC/Spitzer. Among a total of 302 LAEs (224 for $z = 3.1$ and 78 for $z = 3.7$), only 11 (or 4%)

are detected in the K band, i.e., brighter than $K(3\sigma) = 24.1$ mag (AB). Among the 11 K -detected LAEs, eight are spectroscopically confirmed. In our stellar population analysis, we treat K -detected objects individually, while we stack K -undetected objects at each redshift to derive an average SED. Since the vast majority (96%) are undetected in K , the SEDs constructed from stacking should closely represent the whole LAE population at each redshift. We treat the LAEs at $z = 3.1$ and 3.7 collectively as objects at $z \sim 3$, without discussing possible evolution between the two redshifts. Our LAE sample, based on deep optical and near-infrared data over a wide sky area, enables us not only to place strong constraints on the average properties of LAEs by stacking of many objects, but also to study rare, massive LAEs visible in K . We fit stellar population synthesis models to the multi-band photometry of K -detected and K -undetected (stacked) objects, to derive their stellar masses, star formation rates, ages, and dust extinctions. We assume a constant star formation rate and fix the metallicity to $Z = 0.2Z_{\odot}$.

Our main results are as follows:

(i) The K -detected objects have stellar masses of $M_{\text{star}} \sim 10^9 - 10^{10.5} M_{\odot}$, while the K -undetected objects are 1 – 2 orders of magnitude less massive, with $M_{\text{star}} \sim 10^8 - 10^{8.5} M_{\odot}$.

(ii) The K -detected objects are distributed in a similar region in the M_{star} versus M_V plane to spectroscopically confirmed Lyman-break galaxies (LBGs) at $z \sim 3$, while the K -undetected objects have lower M_{star}/L_V ratios and bluer

$M_{1500} - M_V$ colours than the K -detected ones (Figure 7 and the left panel of Figure 8).

(iii) The star formation rates (SFR) of K -detected objects span a wide range of $10 - 10^4 M_\odot \text{ yr}^{-1}$, while those of K -undetected objects fall between $1 - 100 M_\odot \text{ yr}^{-1}$.

(iv) There could be a bimodality in the age distribution among the K -detected objects (Figure 6). The ages of the K -undetected LAEs are around the median value of the ages of the K -detected LAEs.

(v) Four of the K -detected objects have extremely large $E(B - V)_*$, and thus their SFRs derived from rest-frame 1500 Å continua and from Lyman α luminosities are both underestimated by more than two orders of magnitude (Figure 9). On the other hand, the dust extinction of K -undetected objects is modest.

(vi) The Lyman α equivalent width (EW) weakly anticorrelates with M_{star} , except for the four dusty objects having large EWs (Figure 10). No significant correlation is seen between $\text{EW}(\text{Ly}\alpha)$ and $E(B - V)_*$ (Figure 10).

(vii) The Lyman α escape fraction decreases with $E(B - V)_{\text{gas}}$. At a fixed $E(B - V)_{\text{gas}}$, the escape fraction of our LAEs is higher than those of LBGs and local star-forming galaxies (Figure 11).

(viii) The stellar masses and the specific star formation rates (sSFR) of LAEs are compared with those of LBGs, DRGs, SMGs, and galaxies with photometric redshifts of $z_{\text{phot}} \sim 3$. It is found that the LAE population as a whole is the least massive among these galaxy populations, but with relatively high sSFRs (Figure 12).

(ix) Four of our K -detected LAEs with the reddest SEDs, two of which are spectroscopically confirmed, are heavily obscured with $E(B - V)_* \sim 0.65$, and their continua resemble that of Arp 220 and the local ULIRG (Figure 14). They have very high sSFRs in spite of their large stellar masses (Figure 12), and one of them are detected in the MIPS $24\mu\text{m}$ image, which supports the SED-fitting result of SFR. These facts suggest that the red LAEs are massive, dusty starburst galaxies. Our study demonstrates that wide-field Lyman α surveys can detect such dusty starburst galaxies.

ACKNOWLEDGEMENTS

We would like to thank the anonymous referee for very constructive comments and suggestions. We are also very grateful to Gustavo Bruzual and Stéphane Charlot for sending us their new GALAXEV and stellar libraries; to Peter Capak for telling us the information on the SEDs of their SMGs; to Kristen Coppin for providing the SED of the Ly α -emitting SMG; to Georg Feulner for telling us the webpage containing their photometric redshift catalogue; to Steven Finkelstein for sending us the data on the SFRs of their LAEs derived from the best-fit SEDs. RM would like to acknowledge the funding of the Royal Society.

Facilities: Subaru (Suprime-Cam), Magellan: Baade (IMACS), UKIRT (WFCAM), Spitzer (IRAC, MIPS)

REFERENCES

- Atek, H., et al. 2008, *A&A*, 488, 491
 Borys, C., et al. 2005, *ApJ*, 635, 853
 Bruzual, G., & Charlot, S. 1993, *ApJ*, 405, 538
 Bruzual, G., & Charlot, S. 2003, *MNRAS*, 344, 1000
 Bruzual, G. 2007, in *From Stars to Galaxies: Building the Pieces to Build Up the Universe*, ed. A. Vallenari, R. Tantalo, L. Portinari, & A. Moretti, *ASP Conf. Ser.*, 374, 303
 Brocklehurst, M. 1971, *MNRAS*, 153, 471
 Calzetti, D., et al. 1994, *ApJ*, 429, 582
 Calzetti, D., et al. 1997, *AJ*, 114, 1834
 Calzetti, D., et al. 2000, *ApJ*, 533, 682
 Capak, P., et al. 2008, *ApJ*, 681, L53
 Castro Cerón, J. M., et al. 2008, preprint (arXiv:0803.2235)
 Chapman, S. C., et al. 2005, *ApJ*, 622, 772
 Charlot, S., & Fall, S. M. 2000, *ApJ*, 539, 718
 Chary, R.-R., et al. 2005, *ApJ*, 635, L5
 Coppin, K. E. K., et al. 2006, *MNRAS*, 372, 1621
 Coppin, K. E. K., et al. 2009, *MNRAS*, 395, 1905
 Dawson, S., et al. 2007, *ApJ*, 671, 1227
 Erb, D. K., et al. 2006, *ApJ*, 644, 813
 Feulner, G., et al. 2005, *ApJ*, 633, L9
 Finkelstein, S. L., et al. 2008, *ApJ*, 678, 655
 Finkelstein, S. L., et al. 2009, *ApJ*, 691, 165
 Furusawa, H., et al. 2000, *ApJ*, 534, 624
 Furusawa, H., et al. 2008, *ApJS*, 176, 1
 Gawiser, E., et al. 2006, *ApJ*, 642, L13
 Gawiser, E., et al. 2007, *ApJ*, 671, 278
 Gawiser, E. 2009, *NewAR*, 53, 50
 Geach, J. E., et al. 2009, *ApJ*, 700, 1
 Giavalisco, M., et al. 1996, *ApJ*, 466, 831
 Grazian, A., et al. 2007, *A&A*, 465, 393
 Gronwall, C., et al. 2007, *ApJ*, 667, 79
 Hewett, P. C., et al. 2003, *MNRAS*, 367, 454
 Hopkins, A. M., et al. 2006, *ApJ*, 651, 142
 Hu, E. M., et al. 1998, *ApJ*, 502, L99
 Hu, E. M., et al. 2002, *ApJ*, 568, L75
 Iwata, I., et al. 2005, *A&A*, 440, 881
 Iye, M., et al. 2006, *Nature*, 443, 186
 Kashikawa, N., et al. 2006, *ApJ*, 648, 7
 Kennicutt, R. C., 1983, *ApJ*, 272, 54
 Kennicutt, R. C., 1998, *ApJ*, 498, 541
 Lagache, G., et al. 2003, *MNRAS*, 338, 555
 Lai, K., et al. 2007, *ApJ*, 655, 704
 Lai, K., et al. 2008, *ApJ*, 674, 70
 Lawrence, A., et al. 2007, *MNRAS*, 379, 1599
 Madau, P. 1995, *ApJ*, 441, 18
 Madau, P., et al. 1998, *ApJ*, 498, 106
 Maiolino, R., et al. 2008, *A&A*, 488, 463
 Malhotra, S., & Rhoads, J. E. 2002, *ApJ*, 565, L71
 Malhotra, S., & Rhoads, J. E. 2004, *ApJ*, 617, L5
 Maraston, C. 2005, *MNRAS*, 362, 799
 Moustakas, J., et al. 2006, *ApJ*, 642, 775
 Murayama, T., et al. 2007, *ApJS*, 172, 523
 Neufeld, D. A. 1991, *ApJ*, 370, L85
 Nilsson, K. K., et al. 2007, *A&A*, 471, 71
 Ouchi, M., et al. 2003, *ApJ*, 582, 60
 Ouchi, M., et al. 2004, *ApJ*, 611, 660
 Ouchi, M., et al. 2008, *ApJS*, 176, 301
 Papovich, C., et al. 2001, *ApJ*, 559, 620
 Pentericci, L., et al. 2007, *A&A*, 471, 433

- Pentericci, L., et al. 2009, *A&A*, 494, 553
Pettini, M., et al. 2000, *ApJ*, 528, 96
Pettini, M., et al. 2001, *ApJ*, 554, 981
Pirzkal, N., et al. 2007, *ApJ*, 667, 49
Polletta, M., et al. 2007, *ApJ*, 663, 81
Pozzetti, L., & Mannucci, F. 2000, *MNRAS*, 317, L17
Rhoads, J. E., et al. 2000, *ApJ*, 545, L85
Salpeter, E. E. 1955, *ApJ*, 121, 161
Shapley, A. E., et al. 2001, *ApJ*, 562, 95
Shapley, A. E., et al. 2004, *ApJ*, 612, 108
Shimasaku, K., et al. 2006, *PASJ*, 58, 313
Silva, L., et al. 1998, *ApJ*, 509, 103
Simpson, C., et al. 2006, *MNRAS*, 372, 741
Taniguchi, Y., & Shioya, Y. 2000, *ApJ*, 532, L13
Taniguchi, Y., et al. 2005, *PASJ*, 57, 165
Tapken, C., et al. 2007, *A&A*, 467, 63
Teplitz, H. I., et al. 2000, *ApJ*, 533, L65
Ueda, Y., et al. 2008, *ApJS*, 179, 124
van Dokkum, P. G., et al. 2004, *ApJ*, 611, 703
Valls-Gabaud, D. 1993, *ApJ*, 419, 7
Vega, O., et al. 2008, *A&A*, 484, 631
Venemans, B. P., et al. 2005, *A&A*, 431, 793
Verhamme, A., et al. 2008, *A&A*, 491, 89
Warren, S. J., et al. 2007, *MNRAS*, 375, 213
Yoshida, M., et al. 2006, *ApJ*, 653, 988